REPORT DOCUMENTATION PAGE

OMB No. 074-0188

Public reporting burden for this collection of information is estimated to average 1 hour per response, including the time for reviewing instructions, searching existing data sources, gathering and maintaining the data needed, and completing and reviewing this collection of information. Send comments regarding this burden estimate or any other aspect of this collection of information, including suggestions for reducing this burden to Washington Headquarters Services, Directorate for Information Operations and Reports, 1215 Jefferson Davis Highway, Suite 1204, Arlington, VA 22202-4302, and to the Office of Management and Budget, Paperwork Reduction Project (0704-0188), Washington, DC 20503

1. AGENCY USE ONLY (Leave blank)	2. REPORT DATE 05/06/2005	3. REPORT TYPE AND DATES COVERED Final Performance Report, 02/01/03-12/31/04	
4. TITLE AND SUBTITLE Design Tools for Zero Net Mass Flux Devices: CFD Effort		**5. FUNDING NUMBERS** F49620-03-1-0146	
6. AUTHOR(S) Rajat Mittal, PhD			

7. PERFORMING ORGANIZATION NAME(S) AND ADDRESS(ES) The George Washington University 801 22nd St. NW Washington DC 20052	8. PERFORMING ORGANIZATION REPORT NUMBER
9. SPONSORING / MONITORING AGENCY NAME(S) AND ADDRESS(ES) AFOSR 4015 Wilson Boulevard Room 713 Arlington VA 22203-1954 *N A*	**10. SPONSORING / MONITORING AGENCY REPORT NUMBER**

11. SUPPLEMENTARY NOTES

12a. DISTRIBUTION / AVAILABILITY STATEMENT Approved for public release; distribution unlimited.	12b. DISTRIBUTION CODE

13. ABSTRACT *(Maximum 200 Words)*

Numerical simulations have been used to examine the fluid dynamics of zero-net mass flux devices. The emphasis is on extracting insights that can be used in developing simple models of these actuators for use in separation control. The unsteady evolution of a transitional synthetic jet in the absence of cross-flow is investigated by time-accurate three-dimensional direct numerical simulations of incompressible Navier-Stokes equations and the results compared with one of the test cases designated for the *NASA CFD Validation of Synthetic Jets and Turbulent Separation Control*. The validated results are then used for a comprehensive analysis of the flow inside the cavity and the jet slot. The flux of vorticity from these devices is considered to be an important factor in the control of separated flow and in the current study, we have used numerical simulations to extract scaling laws for this quantity. A theoretical model is also proposed for determining the pressure losses in ZNMF slots and orifices and numerical simulations used to determine the scaling of some of the key parameters in this theoretical model.

14. SUBJECT TERMS Flow Control, Synthetic jets, Computational Fluid Dynamics			15. NUMBER OF PAGES 32
			16. PRICE CODE
17. SECURITY CLASSIFICATION OF REPORT Unclassified	**18. SECURITY CLASSIFICATION OF THIS PAGE** Unclassified	**19. SECURITY CLASSIFICATION OF ABSTRACT** Unclassified	**20. LIMITATION OF ABSTRACT** UU

NSN 7540-01-280-5500

7-7-05

20050715 006

I. Objectives

1. Simulate 3-D, incompressible, local interaction of a synthetic jet with a boundary layer. Guidance for test cases will be taken from test cases designated for LaRC workshop on *"CFD Validation of Synthetic Jets and Turbulent Separation Control."*
2. Develop in coordination with experimental team at University of Florida, reduced order models and scaling laws for Zero Net Mass Flux Devices.

II. Introduction

With the onset of MEMS (Micro-Electromechanical Systems) technology the field of active flow control was presented with a promising opportunity of application of the micro/meso devices. Over the past decade ZNMF (Zero-net mass flux) actuators or synthetic jets, as they are popularly known, have emerged as versatile actuators with potential applications ranging from thrust vectoring of jets (Smith & Glezer, 1997), mixing enhancement (Chen et al., 1999; Davis & Glezer, 1999), heat transfer enhancement (Smith et al., 1998; Crook et al., 1999) to triggering turbulence in boundary layers (Rathnasingham & Breuer, 1997, 2003; Lee & Goldstein, 2001) and active flow control (Wygnanski, 1997; Smith et al, 1998b; Amitay et al, 1999; Crook et al., 1999). The versatility of these actuators is primarily attributed to the following reasons: (a) they provide unsteady forcing that is more effective than steady or pulsed forcing, (b) since the jets are synthesized from the working fluid, complex fluid circuits are not required, and (c) actuation frequency can usually be tuned to a particular flow configuration.

A typical synthetic jet actuator consists of a jet orifice opposed on one side by an enclosed cavity consisting of three components: an oscillatory driver, a cavity and an orifice or slot. The oscillating driver compresses and expands the fluid in the cavity by alternating the cavity volume at an exciting frequency to create oscillations. These time-periodic changes in volume of the cavity cause a stream of vortices to be generated at the edges of the orifice, imparting finite momentum into the surrounding fluid, although the net mass-flux through the orifice is zero. Interaction of these vortical structures with the external flow field has been found to cause formation of closed recirculation regions with the modification of the flow boundary, thereby causing global modifications to the base flow on scales larger than the characteristic length scales of the synthetic jets themselves (Smith & Glezer, 1997; Amitay et al, 1997). Both experimental and numerical investigations have been carried out for synthetic jets operating in a quiescent medium and one interacting with an external boundary for afore mentioned applications. However, several questions remained unanswered in terms of the fundamental flow physics governing these flows.

In Section II(a), the unsteady evolution of a transitional synthetic jet in the absence of cross-flow is investigated by time-accurate three-dimensional direct numerical simulations of incompressible Navier-Stokes equations. The flow configuration is similar to the one studied by Yao et al (2004) and the results from the computations are validated using their measurements.

Although numerous parametric studies provide a glimpse of how the actuator performance, depends on geometrical, structural and flow parameters (Rathnasingham & Breuer, 1997; Crook

DISTRIBUTION STATEMENT A
Approved for Public Release
Distribution Unlimited

& Wood, 2001; He et al., 2001; Gallas et al., 2003), one of the key aspects of the design and deployment of these actuators are development of scaling laws. The ongoing parametric studies in collaboration with the experimental studies at the University of Florida have been reported in Section III(b). The flux of vorticity from these devices is considered to be an important factor in the control of separated flow. In the current study we have used numerical simulations to extract scaling laws for this quantity and this study is discussed in Section III(c).

One of the key aspects of low dimensional modeling of these actuators is the pressure loss across the orifice. Depending on the Reynolds number, the pressure losses might be linear or non-linear (Gallas et al., 2004). These losses are however difficult to measure experimentally and numerical simulations provide an excellent way of analyzing the same. Here we use our simulations to examine various aspects of these pressure losses. A theoretical model has been used in order to simplify the governing equations and numerical approach is used to evaluate the unknown coefficients.

III. Accomplishments

a. Numerical Study of a Transitional Synthetic Jet in Quiescent Flow

The formation of zero-net-mass-flux (ZNMF) synthetic jets from a cavity is modeled by the unsteady, incompressible Navier-Stokes equations, written in tensor form as

$$\frac{\partial u_i}{\partial x_i} = 0$$

$$\frac{\partial u_i}{\partial t} + \frac{\partial(u_i u_j)}{\partial x_j} = -\frac{\partial p}{\partial x_i} + \frac{1}{Re}\frac{\partial^2 u_i}{\partial x_j \partial x_j}$$

where the indices, $i = 1, 2, 3$, represent the x_1 (x), x_2 (y), x_3 (z) directions, respectively, p is the pressure and the components of the velocity vector u are denoted by u_1 (u), u_2 (v) and u_3 (w), respectively. The equations are non-dimensionalized with the appropriate length and velocity scales where Re represents the Reynolds number. The Navier-Stokes equations are discretized using a cell-centered, collocated (non-staggered) arrangement of the primitive variables (u, p). In addition to the cell-center velocities (u), the face-center velocities (U), are also computed. Similar to a fully staggered arrangement, only the component normal to the cell-face is calculated and stored. The face-center velocity is used for computing the volume flux from each cell. The advantage of separately computing the face-center velocities has been initially proposed by Zang, Street and Koseff (1994) and discussed in the context of the current method in Ye at al (2004). The equations are integrated in time using a second-order accurate fractional step method. In the first step, the pressure field is computed by solving a Poisson equation. A second-order Adams-Bashforth scheme is employed for the convective terms while the diffusion terms are discretized using an implicit Crank-Nicolson scheme which eliminates the viscous stability constraint. The pressure Poisson equation is solved with a Krylov-based approach. The solver uses weighted-averaging of second order central difference scheme and second order upwind scheme for the discretization of convective face velocities. The QUICK scheme (Leonard, 1979) obtained by setting the weighting factor $\theta = 1/8$ is used in some of the present computations.

3

Care has been taken to ensure that the discretized equations satisfy local and global mass conservation constraints as well as pressure-velocity compatibility relations. The code has been rigorously validated by comparisons of several test cases against established experimental and computational data. Details have been presented elsewhere (Najjar & Mittal, 2003; Bozkurttas et al., 2005).

The geometry used in the computations is relatively simple as compared to the apparatus used in the experiments. In the computations, the shape of the cavity is approximated to be a rectangular box without taking into consideration the finer details that make up the interior of the cavity used in the experiments. Previous numerical studies by Utturkar *et al* (2003) on the sensitivity of the synthetic jets to the design of the jet cavity have shown that the large differences in the internal cavity flow, with symmetric forcing, do not translate into similar differences in the external flow. A schematic of the geometry used in the simulations is shown in figure 1 and it consists of a rectangular cavity connected to the external domain through a narrow rectangular orifice or slot. The origin of the coordinate system is fixed in the jet exit plane along the jet centerline in the symmetry plane. Note that x, y and z are in the cross stream, streamwise and spanwise directions, respectively. While the cavity is defined by the width (W) and height (H), the jet slot is characterized by width (d) and height (h). Care has been taken to match, as closely as possible, the geometrical parameters such as the ratios h/d and W/d used in the computations with those in the experiments. However, it should be noted that cavity height (H) and the slot height (h) can not be properly defined in the experiments of Yao *et al* (2004) as the width varies gradually from W in the cavity to d at the slot exit. Also, it should be noted that the experiments were carried out using a finite aspect ratio jet slot (aspect ratio of 28) in an enclosed box causing the measurements in the symmetry plane to be affected by the end-wall effects of the slot and domain size effects within short distances from the jet exit plane. In the present study, the ratios h/d, W/d and H/d are chosen to be 2.6, 2.45 and 4.95, respectively. In the experiments, the fluid is periodically expelled from and entrained into the cavity by an oscillating diaphragm mounted on one of the side walls of the cavity. The diaphragm oscillation is modeled in the computations by specifying sinusoidal velocity boundary condition $V_0 \sin 2\pi ft$ at the bottom of the cavity. While V_0 is determined by trying to match Re in the experiments, the frequency f is determined by matching St used in the experiments. The effects of three-dimensionality, grid resolution and spanwise domain size on the predictions are studied systematically by a sequence of computations detailed in Table 1.

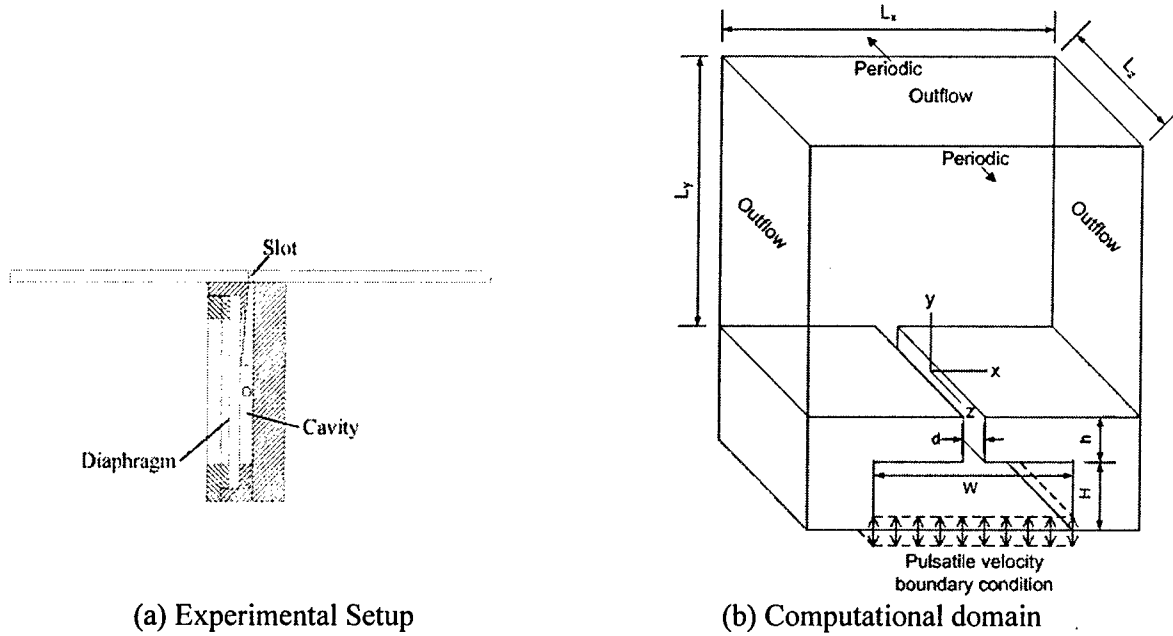(a) Experimental Setup   (b) Computational domain

Figure 1: Schematic of the geometry.

Figure 1 shows the boundary conditions used in the computations. An outflow velocity boundary condition is prescribed on the east, west and north boundaries to allow them to respond freely to the flow created by the jet, and periodic boundary conditions are prescribed in the spanwise (z) direction. The periodicity in the span is intended to model the spanwise homogeneous flow through a slot with an infinite spanwise extent. Figures 2a and 2b show, respectively, the domain mesh and an x-y slice of a typical three-dimensional mesh used in the slot region in the computations. Grids used in the current work are non-uniform in both x- and y-directions, and uniform in the spanwise (z) direction. Sufficient clustering is provided in the slot-region (figure 2c) along x- and y-directions to resolve the vortex structures that form at the slot exit, as well as the shear layer in the slot. Typically 32x55 grid points are used across the slot. A time step corresponding to 14,000 steps per cycle is employed in the calculations. The computations are performed on a single 2.8 GHz Pentium® 4 processor-based workstation and the CPU time incurred for Case 4 was around 270 hours per cycle. The three-dimensionality in the solution is instigated by introducing a small sinusoidal spatial perturbation in the w-velocity over a few hundred time-steps in the first cycle, and thereafter the three-dimensionality is allowed to develop on its own through the inherent instability of the flow. The solution was allowed to evolve for several cycles to eliminate transient effects, and only the later cycles detailed in Table 1 were used in the computation of flow statistics defined below.

(a) Domain grid   (b) Grid in x-y plane   (c) Grid in the slot region
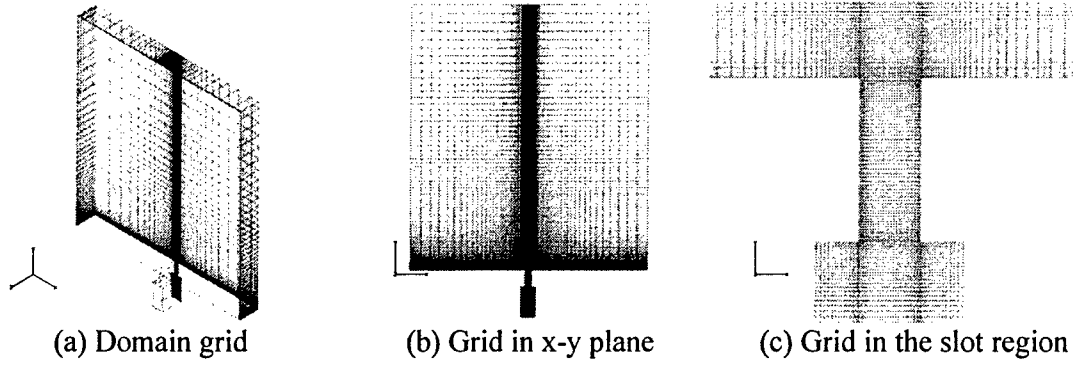
Figure 2: Typical computational mesh used in the simulations.

The various averaging operations employed in the computation of flow statistics in the current study are described as follows. For a generic flow variable $f(\vec{x}, t)$, the time-mean over M cycles is defined as

$$\langle f \rangle(x, y) = \frac{1}{L_z} \frac{1}{MT} \int_{t_0}^{t_0 + MT} \int_0^{L_z} f(\vec{x}, t) \, dz \, dt,$$

where t_0 corresponds to the initial time of the averaging process. Deviation from the time-mean is computed as

$$f'(\vec{x}, t) = f(\vec{x}, t) - \langle f \rangle.$$

In addition, for flows with imposed periodic forcing such as the one under investigation here, it is useful to compute a phase average (Reynolds, 1972). The phase average over M cycles is defined as

$$F(x, y, t) = \frac{1}{L_z} \frac{1}{M} \sum_{n=0}^{M-1} \int_0^{L_z} f(\vec{x}, t + nT) \, dz.$$

Deviation from this phase average is referred to as `turbulent' fluctuation and is computed as
$$f''(\vec{x}, t) = f(\vec{x}, t) - F.$$

The phase average F represents the time-varying coherent (or deterministic) part of the flow and primarily contains time scales directly associated with the organized wave motion. The deviation from the phase average f'' represents the non-deterministic motions and therefore this decomposition provides a means for extracting scales that are associated with the pulsation from a background field of finite turbulent fluctuations.

Case	$L_x \times L_y \times L_z$	$N_x \times N_y \times N_z$	Cycles Averaged
1	40d x 42.45d x 3.0d	132x 220 x 16	10-15
2	40d x 42.45d x 3.0d	132 x 220 x 24	9-15
3	40d x 42.45d x 4.5d	132 x 220x 24	9-13
4	60d x 60d x 6.0d	142 x 230 x 48	5-7
Table 1. Various computations reported in the current study. L_x, L_y and L_z denote the domain size in x-, y- and z-directions, respectively. N_x, N_y and N_z denote the number of cells in x-, y- and z-directions, respectively.			

Contours of phase-averaged spanwise vorticity (Ω_z) obtained for Case 4 are plotted in figure 3 as a function of phase angle φ for every 45°. Phase angle $\varphi = 0°$ is arbitrarily chosen to correspond to the commencement of the upward motion of the diaphragm modeled here by the pulsatile velocity boundary condition at the bottom of the cavity. The horizontal lines seen in the background above the jet exit plane are separated from each other and from the slot exit by distance d. At $\varphi = 0°$, the plot shows some remnants of the previous vortex pair in the near-field and the separation of the shear layer in the interior of the slot caused by the suction of the ambient fluid into the cavity before the upward motion of the diaphragm began. The plot also shows the presence of corner vortices in the cavity. At 45° in phase, a new vortex pair rolls up at the edges of the slot and its size is of the order of the slot width. The plot also shows separation of the shear layer at the inner edges of the slot. When the rollup process is completed at the maximum-expulsion phase of 90°, the vortex pair detaches from the exit plane and grows in size as it advects downstream. At $\varphi = 135°$, small-scale structures begin to appear on the rim of vortex pairs. Also, the rollup of the shear layer at the inner lip of the slot advects downstream leading to Kelvin-Helmholtz-type instabilities that mark the first stage in the transition process. The expulsion phase is completed and the ingestion phase is commenced at $\varphi = 180°$, by which time the vortex pair has advected sufficiently downstream ($y/d \approx 4$) that it is not affected by the suction of ambient fluid into the cavity. At this juncture, the vortex pair loses coherence and begins to mix with the ambient fluid. At $\varphi \approx 225°$, the vortices lose their individual identity, and the suction generates vortex rollup in the interior of the cavity. At maximum-ingestion phase of 270°, the mixing of the primary vortex pair is complete, resulting in a fully developed turbulent jet beyond $y/d = 3$. The vortex pair inside the cavity as seen at $\varphi = 315°$ starts to grow in size while it descends and engulfs the cavity before the next cycle is begun.

Figure 4 depicts a sequence of plots of isosurfaces of vorticity magnitude obtained for Case 4 during the seventh cycle for every 45° in phase. The figure clearly depicts the process of transition of the primary vortex pair into a fully developed turbulent jet. At the maximum-expulsion phase of 90°, the plot shows the presence of spanwise-periodic counter-rotating rib-like vortical structures in the streamwise direction. These streamwise rollers coil around the cores of the primary vortex pair. As the primary vortex pair advects downstream in the subsequent phases, these spanwise instabilities undergo rapid amplification leading to breakdown of the primary vortex pair due to three-dimensional vortex stretching and complete mixing of the vortices with the ambient fluid within a short distance from the orifice. This process of transition is consistent with the phase-locked smoke visualizations of a synthetic jet at Re = 766 by Smith and Glezer (1998a).
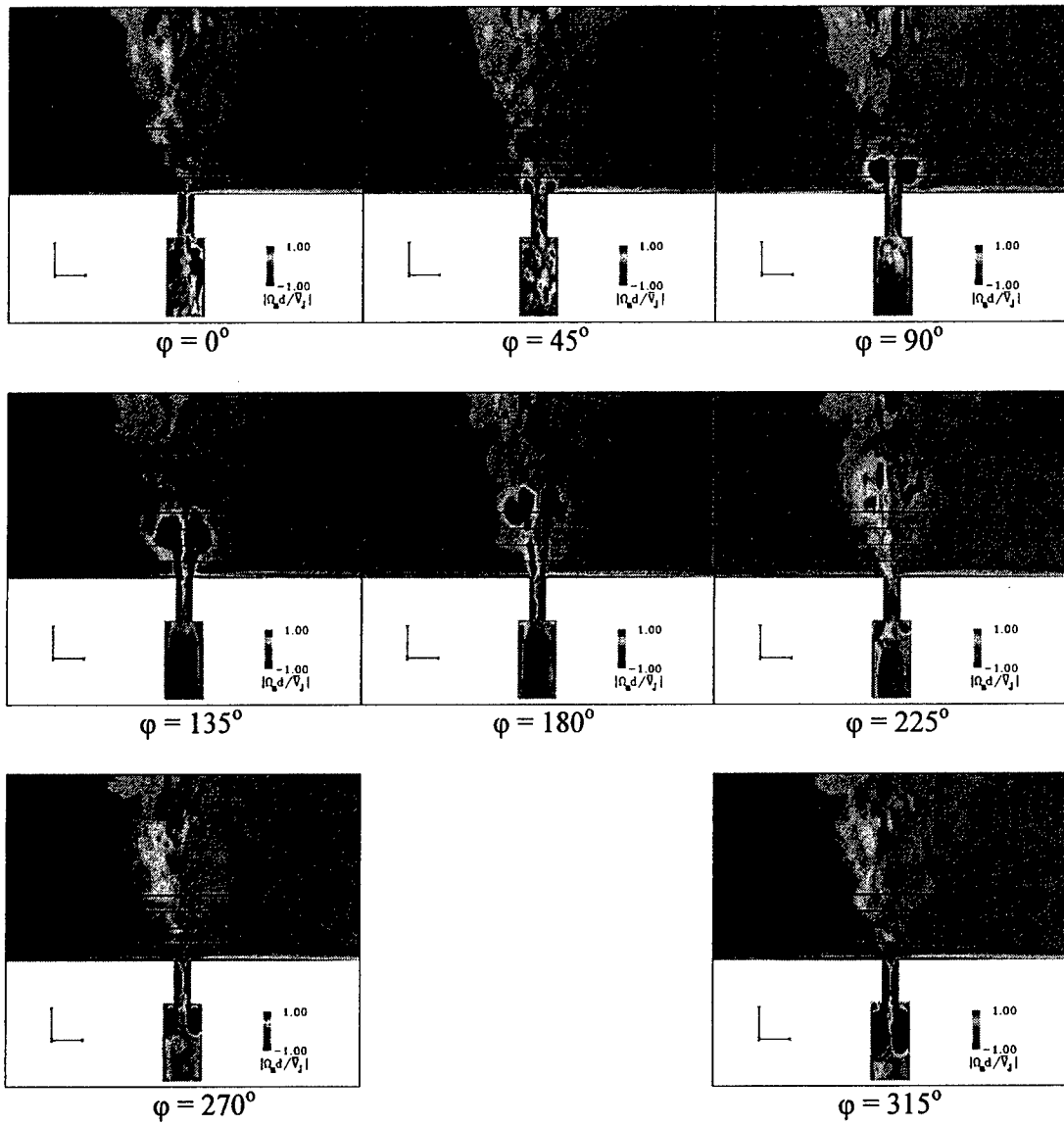
Figure 3: Contours of phase-averaged spanwise vorticity (Ω_z) at various phase angles obtained for Case 4.
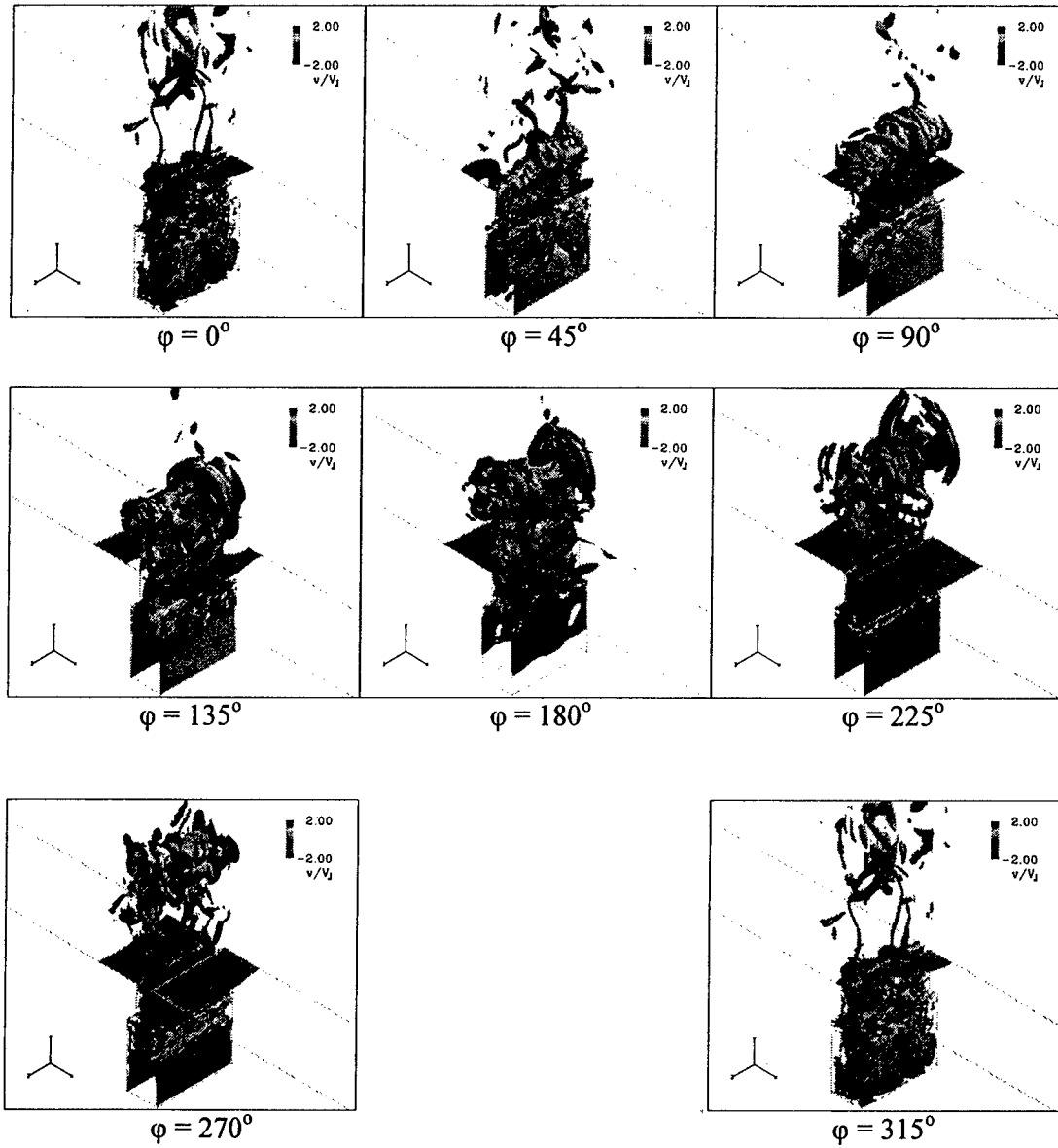
Figure 5: Isosurfaces of instantaneous vorticity magnitude colored by v-velocity at various phase angles obtained for Case 4 during the seventh cycle.

Plot of phase-averaged time history of v-velocity obtained from the computations along the vertical centerline at $y/d = 0.1$ is shown in figure 5. Also included in this plot are the PIV and the LDV measurements of Yao et al (2004). Whereas the computed results show grid convergence, the PIV and LDV measurements show differences amongst themselves with respect to the peak amplitudes and alignment in phase. Even though the PIV data align with the computations at maximum-ingestion phase ($\varphi = 270°$), the maximum-expulsion in the PIV measurements leads the computational results by as much as $14°$ in phase. Nevertheless, in the comparisons of cross stream distributions of various velocity profiles, the results from the simulations at maximum-

expulsion phase are validated against the PIV data at $\varphi = 90°$ rather than at $\varphi = 76°$ as the agreement is better at $\varphi = 90°$ (not shown here) than at $\varphi = 76°$.
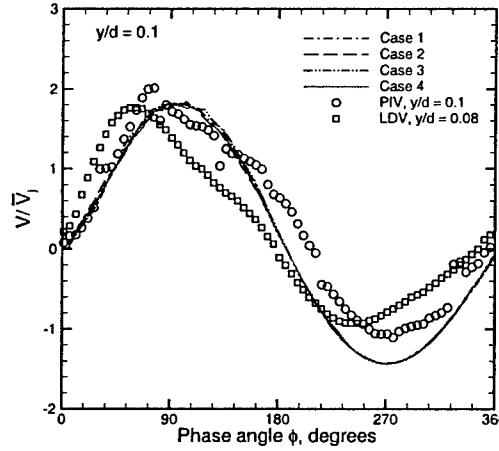

Figure 5: Plot of phase-averaged v-velocity along the vertical centerline at $y/d = 0.1$.

Figure 6 shows the plots of phase-averaged v-velocity profile along the centerline $x/d = 0.0$ above the jet exit plane at phase angles $\varphi \approx 90°$ and $\varphi \approx 270°$. At the maximum-expulsion phase ($\varphi \approx 90°$), the computed velocity profiles closely agree with the measurements for $y/d \geq 2$, and for $y/d < 2$ the magnitude of the maximum centerline velocity in the computations takes a slightly lower value than the measurements. This difference can be attributed to the end wall effects in the experiments that cause the fluid to accelerate between shear layers formed at the slot end walls. At the maximum-ingestion phase, results from the computations match the measurements until up to $y/d = 4$ beyond which the computations show higher velocity magnitude than the measurements. Figure 7 shows the comparisons with the measurements of the cross stream distributions of phase-averaged u- and v-velocity profiles above the jet exit plane at $y/d = 0.787$, 1.575 and 2.362 at $\varphi \approx 90°$.
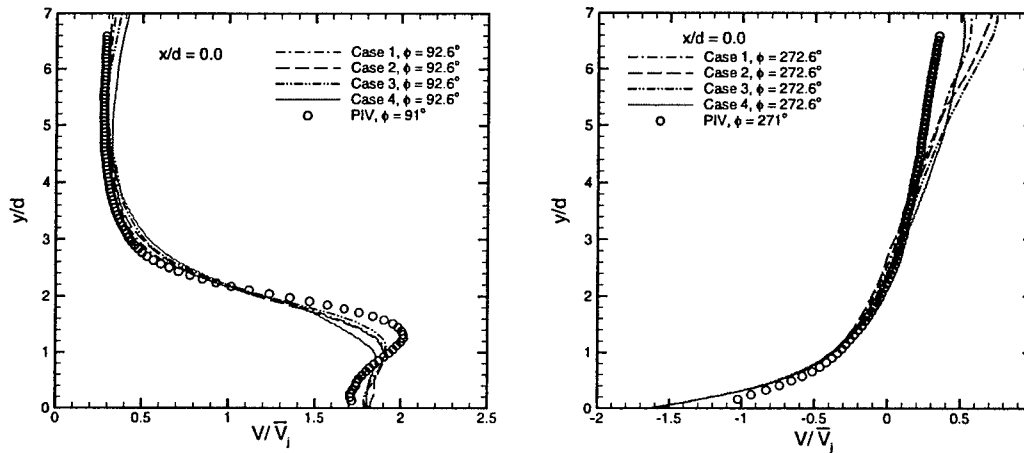

Figure 6: Plot of phase-averaged v-velocity profile along the vertical centerline $x/d=0.0$ above the jet exit plane at phase angles $\varphi \approx 90°$ and $\varphi \approx 270°$.
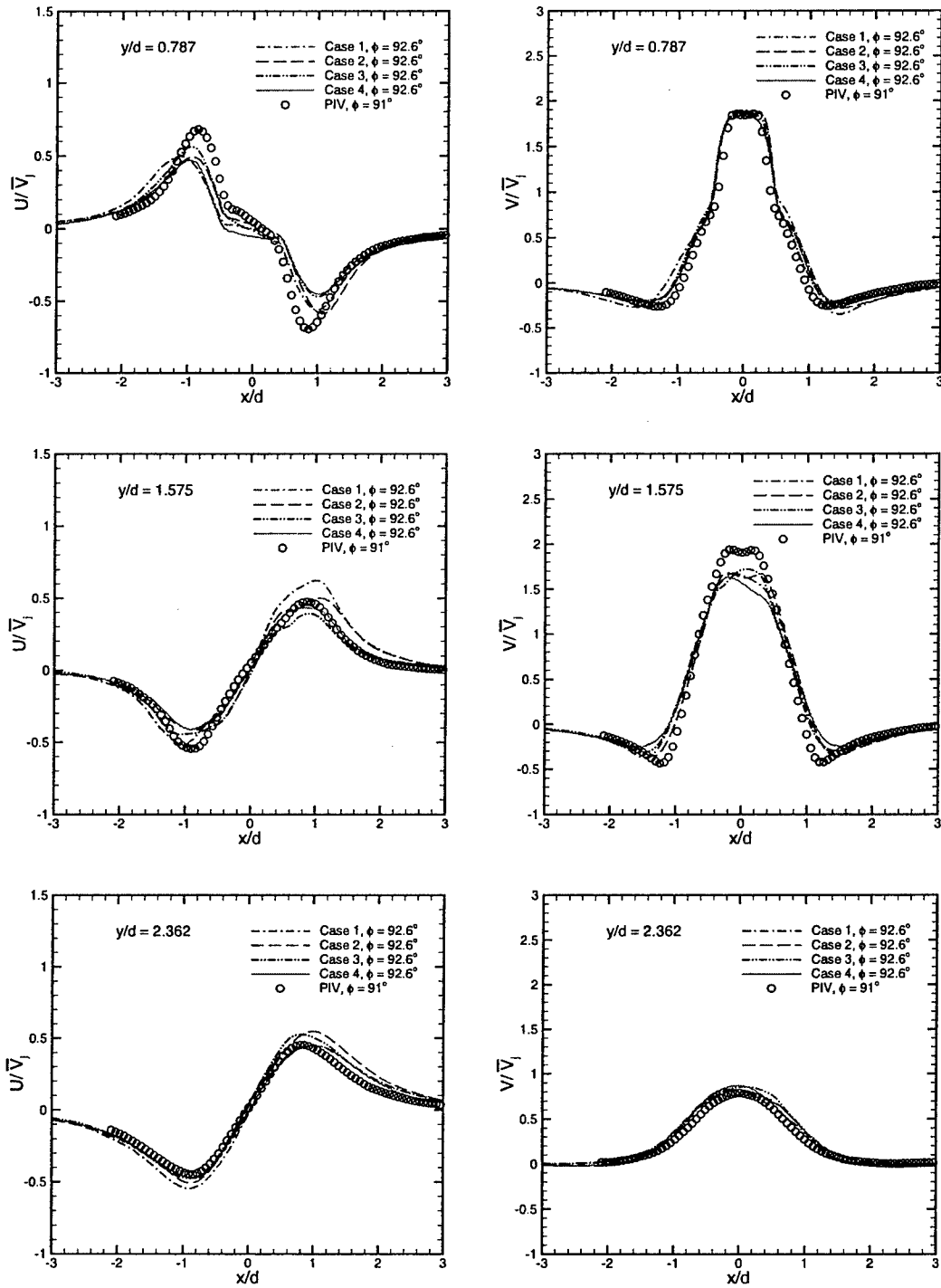
10

Figure 7: Plot of phase-averaged *u*- and *v*-velocity profiles along the horizontal lines *y/d* = 0.787, *y/d* = 1.574 and *y/d* = 2.362, above the jet exit plane at phase angle φ ≈ 90°.
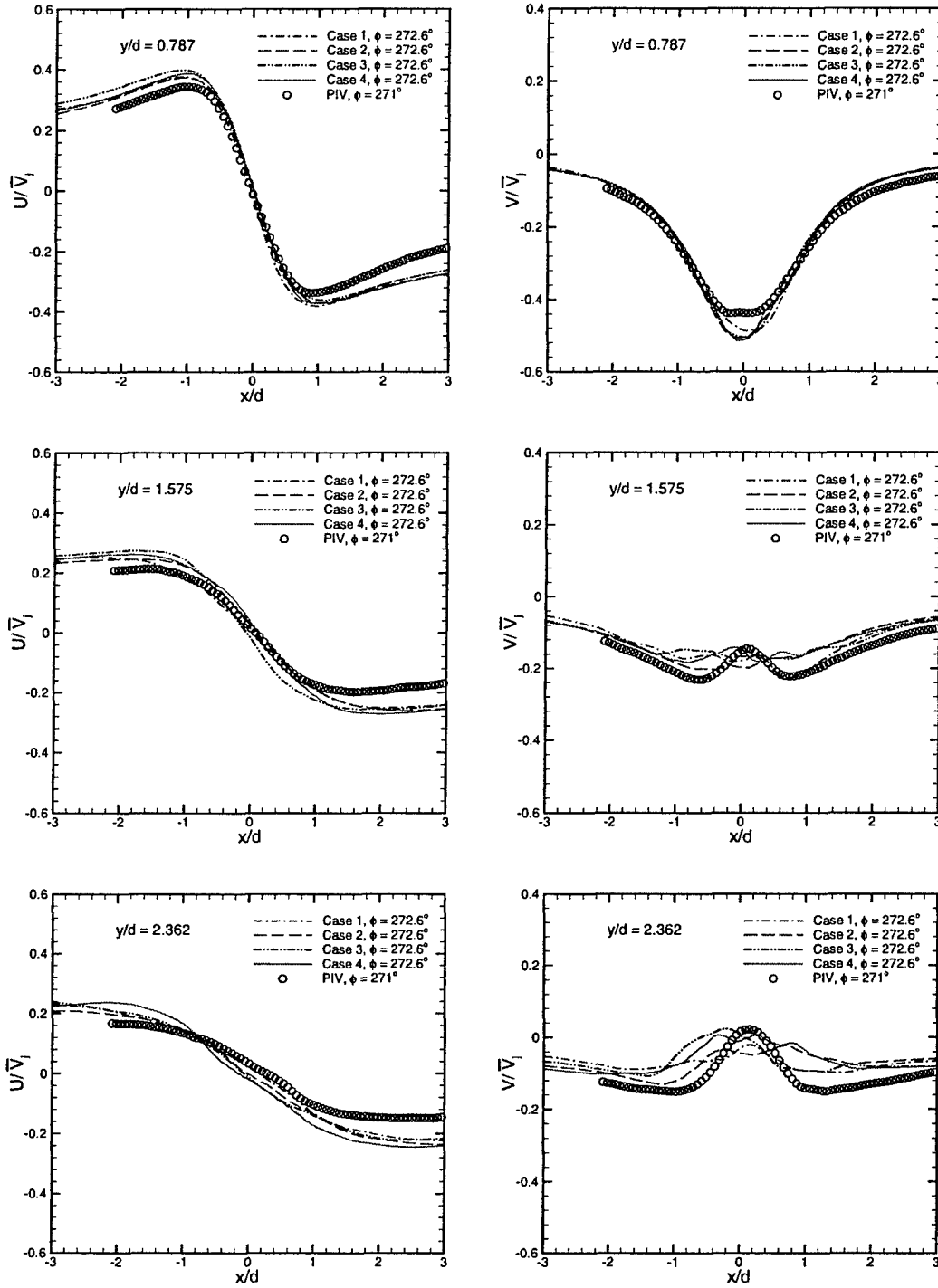
Figure 8: Plot of phase-averaged *u-* and *v*-velocity profiles along the horizontal lines y/d = 0.787, y/d = 1.574 and y/d = 2.362, above the jet exit plane at phase angle $\varphi \approx 270°$.

Except for the lower values of the maxima and the minima in the U-velocity at $y/d = 0.787$ and the V-velocity at $y/d = 1.575$ as compared to the measurements, the computed profiles closely agree with the experimental measurements. Similar profiles at phase angle $\varphi = 270°$ is shown in figure 8. At this maximum-ingestion phase, the velocity profiles follow the general trend seen in the measurements. However, the magnitude of the computed U-velocity outside the core region of the jet at all three stations takes a higher value than the measurements, implying greater entrainment in the computed flow fields than that observed in the experiments. Also, the magnitude of V-velocity along the centerline at $y/d = 0.787$ is higher in the computations as compared to the measurements. The jitter seen in the computed V-velocity profiles in the core region at $y/d = 1.575$ and $y/d = 2.362$ is attributed to the lack of a very large sample size as in the experiments for the computation of flow statistics.
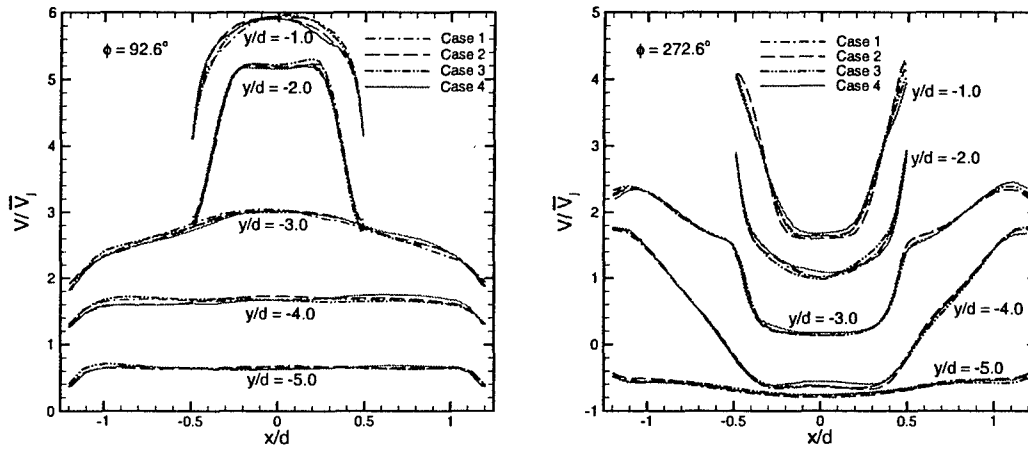

Figure 9: Plot of phase-averaged v-velocity profile along the horizontal lines in the slot $(y/d = -1.0$ and $-2.0)$ and the cavity $(y/d = -3.0, -4.0$ and $-5.0)$ at phase angles $\varphi \approx 90°$ and $\varphi \approx 270°$. Profiles at $y/d = -4.0, -3.0, -2.0$ and -1.0 are shifted up along the ordinate by 1, 2, 3 and 4 units, respectively, from that at $y/d = -5.0$.

Based on these validations in the near-field, we extend the ongoing study to gain insight into the flow field inside the slot and the cavity where experimental measurements are not possible due to limitations on the instrumentation. Figure 9 shows the cross stream distributions of phase-averaged v-velocity profiles from the computations at $\varphi \approx 90°$ and $\varphi \approx 270°$ at five different stations. Whereas the profiles at $y/d \approx -1$ and -2 correspond to stations in the slot, the profiles at $y/d \approx -3, -4$ and -5 correspond to stations in the cavity. At $\varphi \approx 90°$, the cross stream distributions at $y/d \approx -5$ and -4 resemble developed channel flow profiles. The computed profiles at $y/d \approx -3$ show reverse flow near the walls implying the presence of the corner eddy in the cavity. The acceleration of the fluid from the cavity into the slot is expected to cause laminarization of the flow as seen in the profiles at $y/d \approx -2$. The profiles at this station also show reverse flow caused by separation at the inner edges of the slot. However, the profiles become more uniform at $y/d \approx -1$ before the flow exits out of the slot. At the maximum-ingestion phase ($\varphi = 270°$), as seen in the profiles at $y/d \approx -1$, the suction at the slot has a stabilizing effect on the ambient fluid as it accelerates into the narrow slot and so we expect the flow to be less turbulent. This aspect of the

13

flow is looked at in more detail using spectral analysis discussed later. However, the flow recovers the developed profile at $y/d \approx$ -2 before it exits out of the slot and rolls up into a vortex pair in the cavity. Profiles at $y/d \approx$ -3 and -4 show recirculation regions characterized by the vortex pair in the cavity. At $y/d \approx$ -5, the profiles do not show any flow reversals as this station is not within the reach of the vortex pair at this instant in phase.
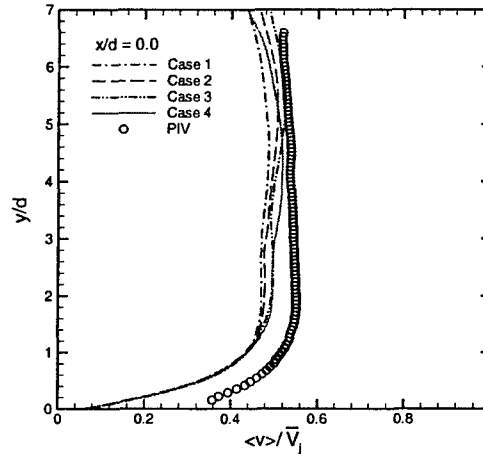

Figure 10: Plot of time-averaged v-velocity profile along the vertical centerline $x/d = 0.0$ above the jet exit plane.

Figure 10 shows the comparisons of the computed time-averaged v-velocity profiles with the experiments along the vertical centerline above the jet exit plane. The plot shows consistently lower values in the computed profiles as compared to the measurements. The cross stream distributions of the time-averaged u- and v-velocity profiles are shown in figure 11 at three stations ($y/d \approx$ 0.787, 1.575 and 2.362) above the jet exit plane. While the computed $<u>$-velocity profiles consistently show higher values than the measurements outside the core region of the jet at all stations, the computed $<v>$-velocity profiles closely match the experiments except for the lower values along the jet centerline as compared to the measurements. Time-averaged v-velocity profiles at five stations in the slot and the cavity are shown in figure 12. It is interesting to note that while the velocity in the shear layer at $y/d \approx$ -1 is positive, the velocity is negative in the shear layer at $y/d \approx$ -2 implying that somewhere in between these two stations, the mean cross stream distribution is zero across the slot since the net mass flux is zero. In the cavity, $<v>$-velocity is positive in the shear layer at all three stations, whereas it is negative in the core
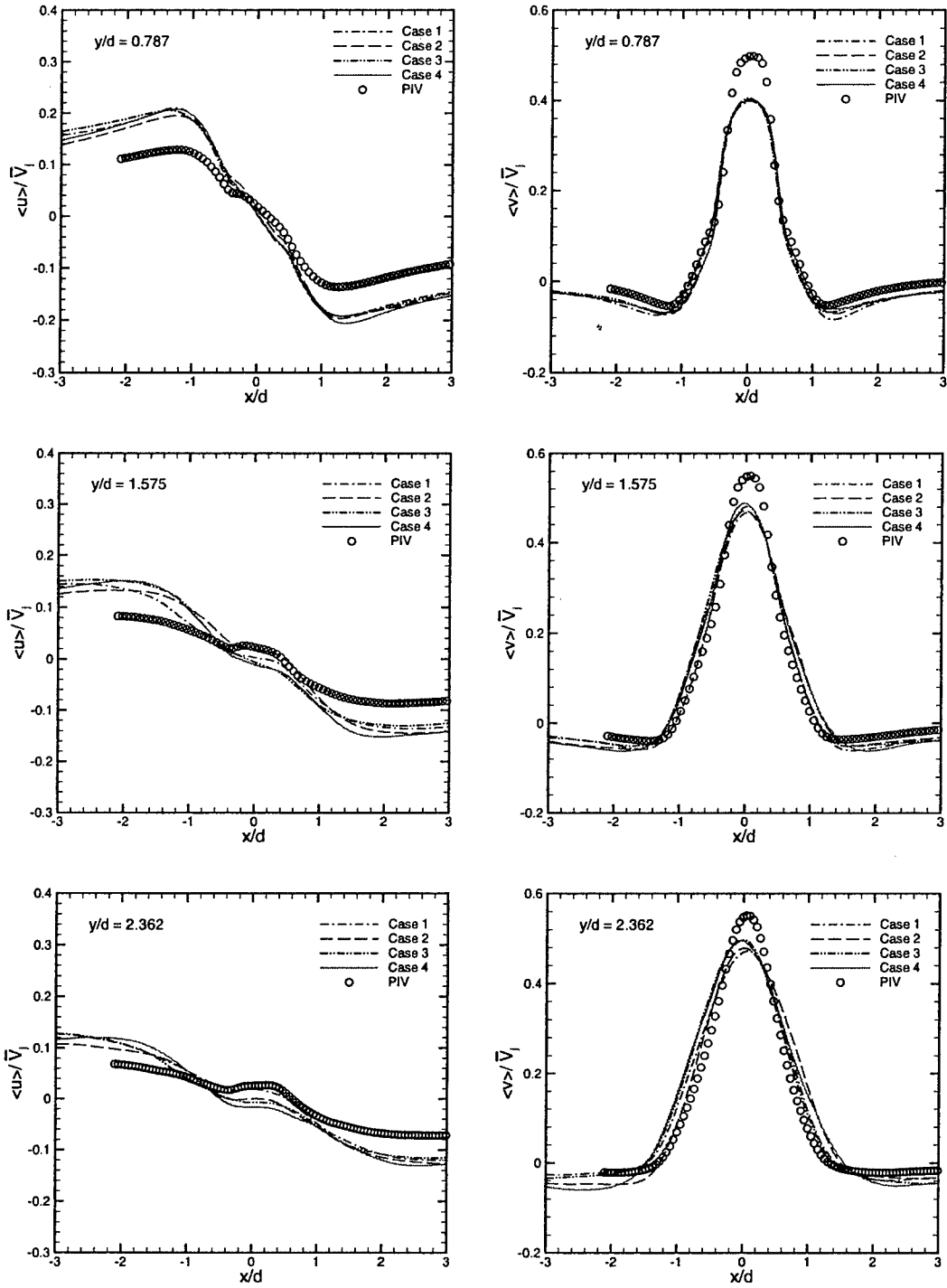
Figure 11: Plot of time-averaged u- and v-velocity profiles along the horizontal lines $y/d = 0.787$, $y/d = 1.574$ and $y/d = 2.362$, above the jet exit plane.
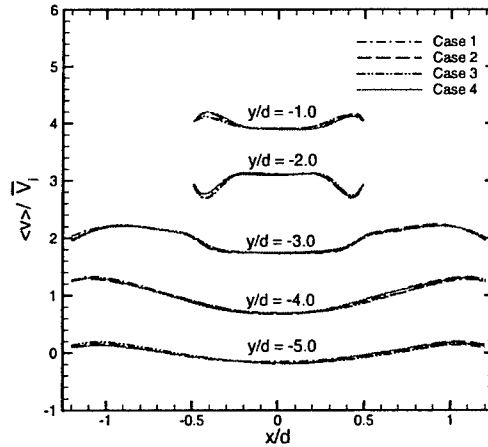
Figure 12: Plot of time-averaged *v*-velocity profile along the horizontal lines in the slot (*y/d* = -1.0 and -2.0) and the cavity (*y/d* = -3.0, -4.0 and -5.0). Profiles at *y/d* = -4.0, -3.0, -2.0 and -1.0 are shifted up along the ordinate by 1, 2, 3 and 4 units, respectively, from that at *y/d* = -5.0.

We now focus on the temporal variations and the frequency spectra of *v*-velocity at several stations along the jet centerline for Case 4. At any given (*x,y*) location, the frequency spectrum is obtained by computing the average of the spectra at several (but not all) grid points in the homogeneous spanwise direction. Figure 13 shows the temporal variations of the streamwise velocity (*v*), the phase averages of the streamwise velocity (*V*) and the corresponding velocity fluctuations (*v''*) at eight different streamwise locations along the jet centerline in the symmetry plane (*z* = 0). The instantaneous streamwise velocity is averaged in 24 phase bins, and the corresponding velocity fluctuations are obtained by subtracting the linearly-interpolated phase averages from the instantaneous velocity. The temporal variations in the near-field (y/d ≈ 0 to 4) show more intense velocity fluctuations (*v''*) during the blowing phase of the cycle than during the suction phase indicating that suction of the ambient fluid into the narrow slot has a tendency to stabilize the flow in the near-field. Also, in the slot (*y/d* ≈ -1 and -2), the velocity variation is mostly sinusoidal and the velocity fluctuations are spread almost uniformly over the entire cycle. Furthermore, the frequency spectra corresponding to the variations of *v''* at these stations are shown in figures 14 and 15. It should be noted that the temporal variations shown in figure 13 correspond to fixed spanwise stations whereas the frequency spectra are obtained by averaging the individual spectra at a particular (*x,y*) location across the span. The frequency ($\omega_\kappa = 2\pi f \kappa$, where κ is the wave number) in these plots is non-dimensionalized by $V_j d$ and the spectrum $E_{vv}(\omega_\kappa)$ is obtained by normalizing the spectral density by $2\pi f$. Also included in these plots are the   lines   corresponding   to $\kappa^{-5/3}$ and κ^{-7} variations. Whereas the $\kappa^{-5/3}$ variation is associated with the inertial subrange (Tennekes 1972), the κ^{-7} variation on the other hand characterizes the dissipation range (Hinze, 1975) where most of the turbulent kinetic energy is dissipated by the action of the viscosity. A noticeable inertial subrange and dissipation range in the spectra at *y/d* ≈ 1, 2 and 3 in figure 14 indicates a well-developed turbulent flow at these stations. Since the Reynolds number is not very large, the dissipating eddies are only slightly smaller than the energy-containing eddies and so the inertial subrange is quite narrow at *y/d* ≈ 0 and broadens as one moves away from the jet exit plane. In the cavity at *y/d* ≈ -4, the spectrum shown in figure 15 depicts a relatively short inertial subrange and a distinct dissipation range associated with the turbulent flow at this station.

16

However, as one moves up towards the slot, the inertial range narrows further and the dissipation range departs from the -7 slope. This is consistent with the earlier observation that flow laminarizes as it accelerates into the slot from the cavity.
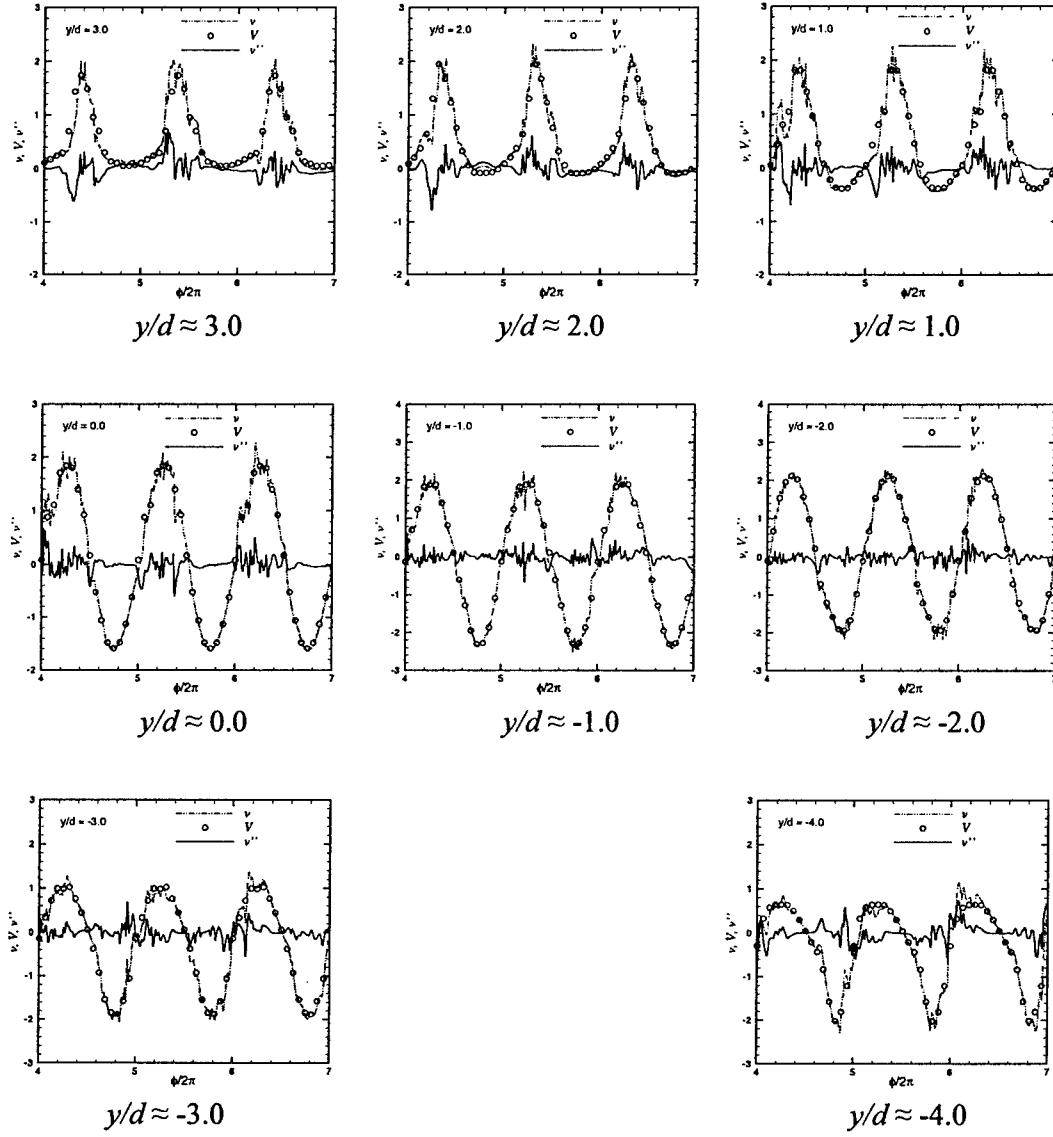

$y/d \approx 3.0$ $y/d \approx 2.0$ $y/d \approx 1.0$

$y/d \approx 0.0$ $y/d \approx -1.0$ $y/d \approx -2.0$

$y/d \approx -3.0$ $y/d \approx -4.0$

Figure 13: Temporal variation of instantaneous v-velocity, phase-averaged v-velocity and turbulent fluctuation v'' obtained for Case 4 at various locations along the centerline in the symmetry plane.
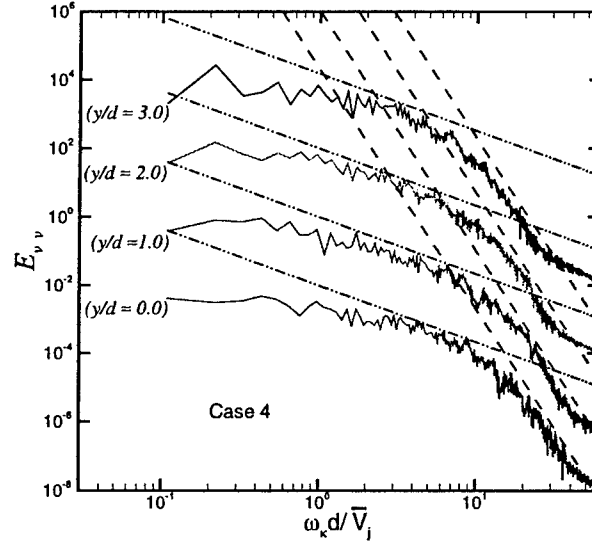
17

Figure 14: Frequency spectra corresponding to turbulent fluctuations v'' along the centerline at $y/d \approx$ 0.0, 1.0, 2.0 and 3.0 for Case 4. Note that the spectrum at $y/d \approx$ 1.0, 2.0 and 3.0 is shifted up by two, four and six decades, respectively, from that at $y/d =$ 0.0. Dash-dot-dot and dashed lines correspond to $\kappa^{-5/3}$ and κ^{-7} variations, respectively.
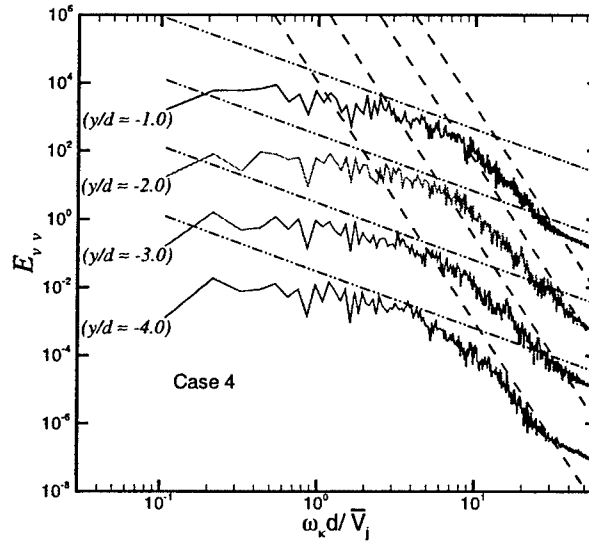

Figure 15: Frequency spectra corresponding to turbulent fluctuations v'' along the centerline at $y/d \approx$ -1.0, -2.0, -3.0 and -4.0 for Case 4. Note that the spectrum at $y/d \approx$ -3.0, -2.0 and -1.0 is shifted up by two, four and six decades, respectively, from that at $y/d =$ -4.0. Dash-dot-dot and dashed lines correspond to $\kappa^{-5/3}$ and κ^{-7} variations, respectively.

18

b. Low Dimensional Modeling of ZNMF Actuators

Ongoing experimental and computational studies are focused on ZNMF actuators in both quiescent and grazing flows; however numerous unresolved issues remain concerning the fundamental governing physics of these devices, effectively hindering their modeling, design and optimization. For example, the unsteady flow in the orifice or slot plays a large role in determining the actuator performance. While numerous parametric studies have examined various orifice geometry and flow conditions, a clear understanding of the loss mechanisms is still lacking. Detailed numerical simulations (and companion experiments) can be used to elucidate the underlying physics but are not practical as a design tool. Instead, accurate low dimensional models are required to facilitate the effective design of ZNMF actuators for specific applications. While the ultimate goal is to develop models suitable for use in boundary layer flow control in which the ZNMF actuator interacts with a grazing flow, the ongoing collaborative effort focuses on experimental and computational efforts to first understand and model the oscillatory orifice flow in the simpler case without a grazing flow. In particular, experimental data and numerical simulations are used to explore the flow behavior and develop components for a low-order lumped element model of more commonly employed *sharp-edged* orifice or slot of a ZNMF actuator. The effects of various governing dimensionless parameters are examined.

Table 2. Test Matrix.

Case	Jet formed	h/d	Re_j	S	h/L_0	ω/ω_H
1	no	1	262	25	0.76	0.13
2	no	2	262	25	1.52	0.09
3	yes	0.68	262	10	0.08	0.18

Table 2 gives the details of the numerical cases studied in quiescent medium while details of the experimental results can be found in Gallas *et al.* (2004). The numerical details are similar to the one mentioned in the previous section. Utilizing data acquired, Figure 16 plots the fluctuating pressure normalized by the dynamic pressure based on the centerline velocity, U_{CL} vs. L_0/h, the ratio of the stroke length to the orifice height. The pressure loss data asymptote to a value of approximately 0.75 as L_0/h increases beyond a value of ~4. This suggests that when the fluid particle excursion or stroke length is much larger than the orifice height h, minor "nonlinear" losses due to entrance and exit effects dominate the flow. However, the magnitude of these losses and the degree of nonlinear distortion is likely to be strongly dependent on Reynolds number. For shorter stroke lengths when the particle excursion is smaller than h, the flow presumably approaches a fully-developed state, and major losses which scale with u' dominate the minor losses. Here, "fully developed" means that there exists a region within the orifice away from either exit, where the velocity profile at a given point during the cycle is not a function of axial position x.
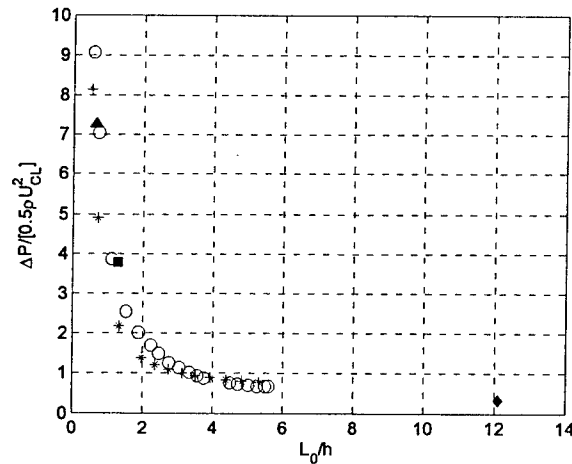
19

Figure 16. Pressure fluctuation normalized by dynamic pressure based on centerline velocity vs. L_0/h: (*) S=8, 9<Re_j<90; (o) S=36, 190<Re_j<1875; (▲) Case 1; (■) Case 2; (♦) Case 3.

The results of the CFD simulations allow us to explore this hypothesis further. Figure 17 shows the variation of the spanwise vorticity for the three computational cases. For Cases 1 & 2, no jet is formed as seen in Fig. 17 (a) and (b). The vorticity contours show that vortices formed during the expulsion cycle for these cases are ingested back during the suction cycle, leading to the trapping of vortices inside the orifice and increased losses over and above that predicted by linear theory. In contrast, clear jet formation occurs for Case 3 as shown in Fig. 17 (c). These results are consistent with the jet formation criterion proposed by Utturkar (2002) and Utturkar et al.(2003), which have shown that jets are formed above a critical value of $Re_j/S^2 > 0.16$ and 1 for a sharp orifice and 2-D slot, respectively. The flow is qualitatively the same for Cases 1 and 2 despite the doubling of h, suggesting that orifice height plays a relatively minor role in determining jet formation.

(a)   (b)   (c)
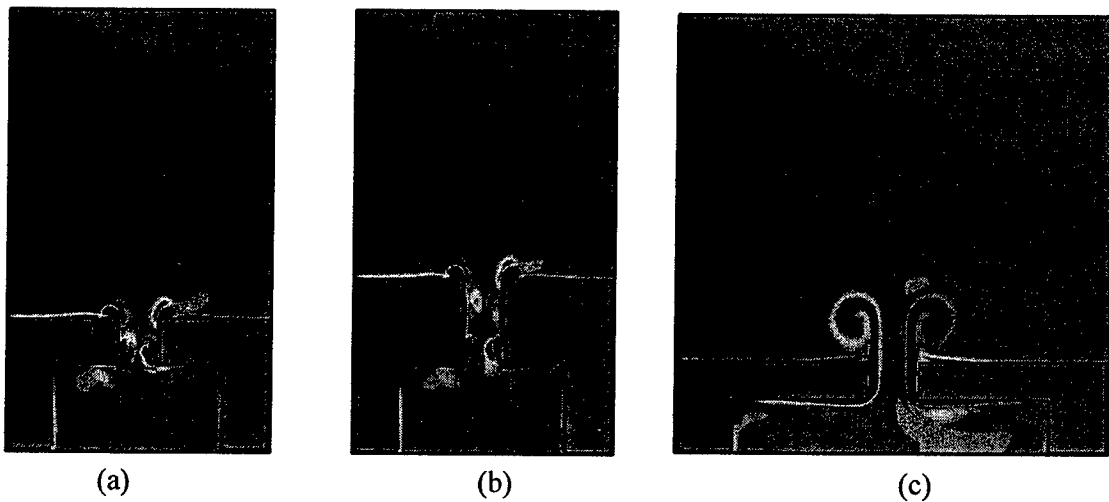
Figure 17. Vorticity contours during the maximum expulsion portion of the cycle for (a) Case 1, (b) Case 2, and (c) Case 3.

Next, temporal variations of the pressure as a function of location along the slot and volume flow rate obtained from the numerical simulations are shown in Figure 18. A comparison of the pressure traces shows a significant phase shift in the pressure (see probe 1 position) in the jet formation case (Case 3) with the largest stroke length compared to Cases 1 and 2. The deviation of the pressure signal from a sinusoidal shape is a clear indication that the periodic ejection and ingestion of strong vortices has a major effect on the resistance characteristics of the orifice. This has been confirmed by the experimental findings (Gallas et al., 2004). However, for the highest Reynolds number experimental results, the nonlinear losses are reduced in magnitude such that the pressure distortion is not evident.
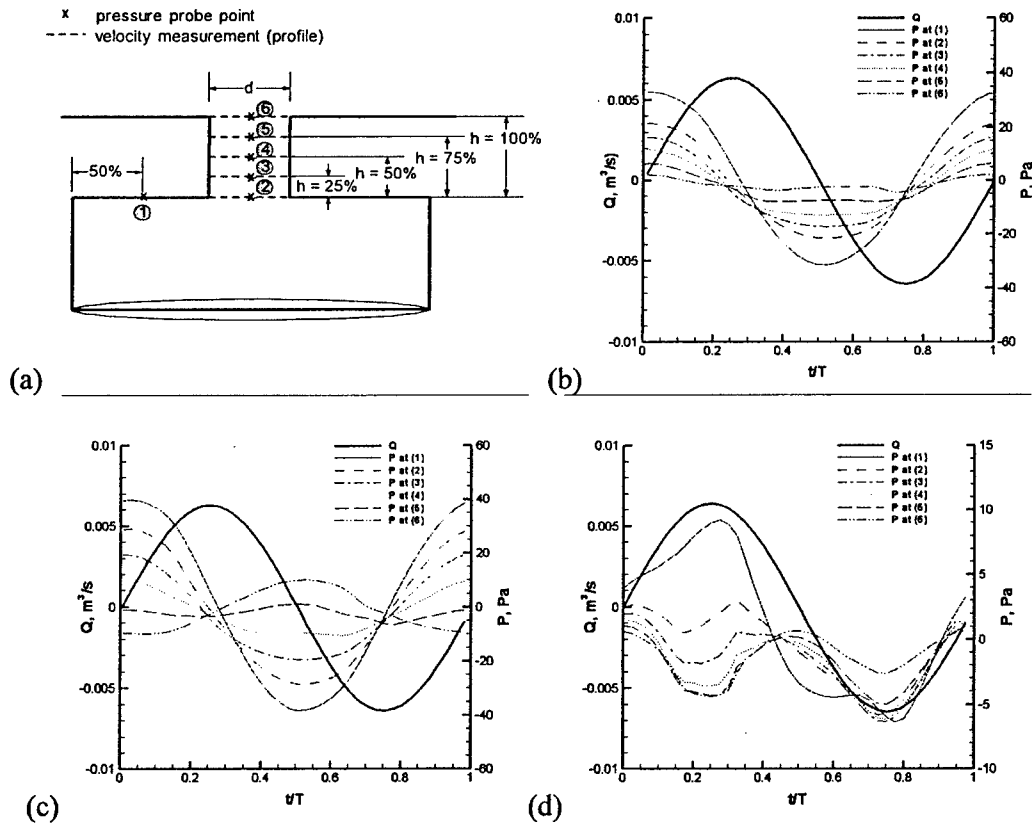

Figure 18. (a) Probe positions in numerical simulations. Volume flow rate/pressure at various locations inside the orifice for (b) Case 1, (c) Case 2 and (d) Case 3 during a cycle. The pressure at probes 2 to 6 are spatially averaged pressure across the orifice.

The CFD data permits the examination of the evolution of the velocity profile inside the slot. Figure 19 shows the computed velocity profiles at various locations in the orifice corresponding to the maximum expulsion phase. As with the pressure, Cases 1 and 2 are qualitatively similar, and both show that the velocity profile undergoes significant development along the length of the slot. A close examination of flow animations reveals the strong periodic influence of the

21

vorticity as it is expelled and then ingested again. This effect is presumably enhanced by the sharp corners of the slot compared to the rounded edges studied by Smith and Swift (2003).In contrast, the evolution of the velocity profiles for Case 3, in which a jet is formed, is significantly different from the previous two cases. For this case, where the stroke length is much larger than the orifice height, the core flow moves in phase at each location inside the orifice. Furthermore, it appears that the flow approaches a quasi-steady behavior for large L_0/h and is dominated by entrance and exit losses, the magnitude of which is inversely proportional to Reynolds number.
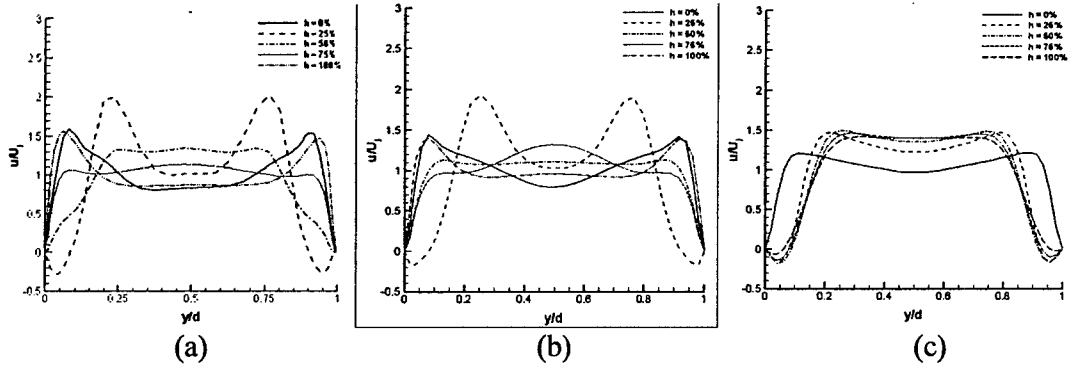

Figure 19. Velocity profile at different location inside the orifice, during the maximum expulsion portion of the cycle. (a) Case 1, (b) Case 2 and (c) Case 3. The locations are indicated in Figure 18(a).

In conclusion the joint experimental and numerical study shows that the flow field emanating from the orifice/slot is characterized by both linear and nonlinear losses. Due to the sharp-edged geometry, the linear losses are under predicted by the theoretical linear solution for pipe/channel flow driven by an oscillating pressure gradient. Furthermore, the flow field inside the orifice may vary significantly from the linear solution due to the persistent presence of vorticity in the orifice from previous expulsion/ingestion cycles. Nevertheless, it was found that the pressure drop in the orifice, when normalized by the dynamic pressure based on the amplitude of the flow centerline velocity, collapsed at high dimensionless stoke lengths over a range of Reynolds and Stokes numbers in the experiments and simulations. When the stroke length is large compared to the orifice height this dimensionless pressure drop is small, presumably because the flow is dominated by nonlinear minor losses associated with entrance effects. However, when the stroke length is small, the pressure drop rises, presumably due to the lower Reynolds numbers and the major losses typical of fully-developed flows.

c. Scaling of Vorticity Flus from Synthetic Jets

In previous studies, a parameter considered key to characterizing the jet is the momentum coefficient C_μ (Amitay et al., 1999; Seifert & Pack, 1999) generally defined as the ratio of the net momentum imparted by the jet over the ejection portion of the cycle to the momentum of the external flow. However, synthetic jets not only impart momentum to the external boundary layer but also expel vortices which lead to mixing and transition of a laminar boundary layer to turbulent boundary layer. A recent study by Yehoshua & Seifert (2000) suggests that the

22

vorticity flux is an important factor for grazing flows. Past simulations and experiments have shown that the vorticity flux is the key aspect that determines the "formation" of synthetic jets in quiescent flow (Utturkar et al., 2003). This flux of vorticity, Ω_v during the expulsion can be defined as,

$$\Omega_v = \int_0^{T/2} \int_0^{d/2} \xi_z u\, dy\, dt$$

where ξ_z is the vorticity component of interest and T is the time period.

It would therefore be useful to develop scaling laws for the vorticity flux of ZNMF jets in grazing flows. Based on previous simulations we propose the following functional dependence as,

$$\frac{\Omega_v}{\overline{V}_J d} = fn(St, \frac{U_\infty}{\overline{V}_J}, \frac{\delta}{d}, Re_J)$$
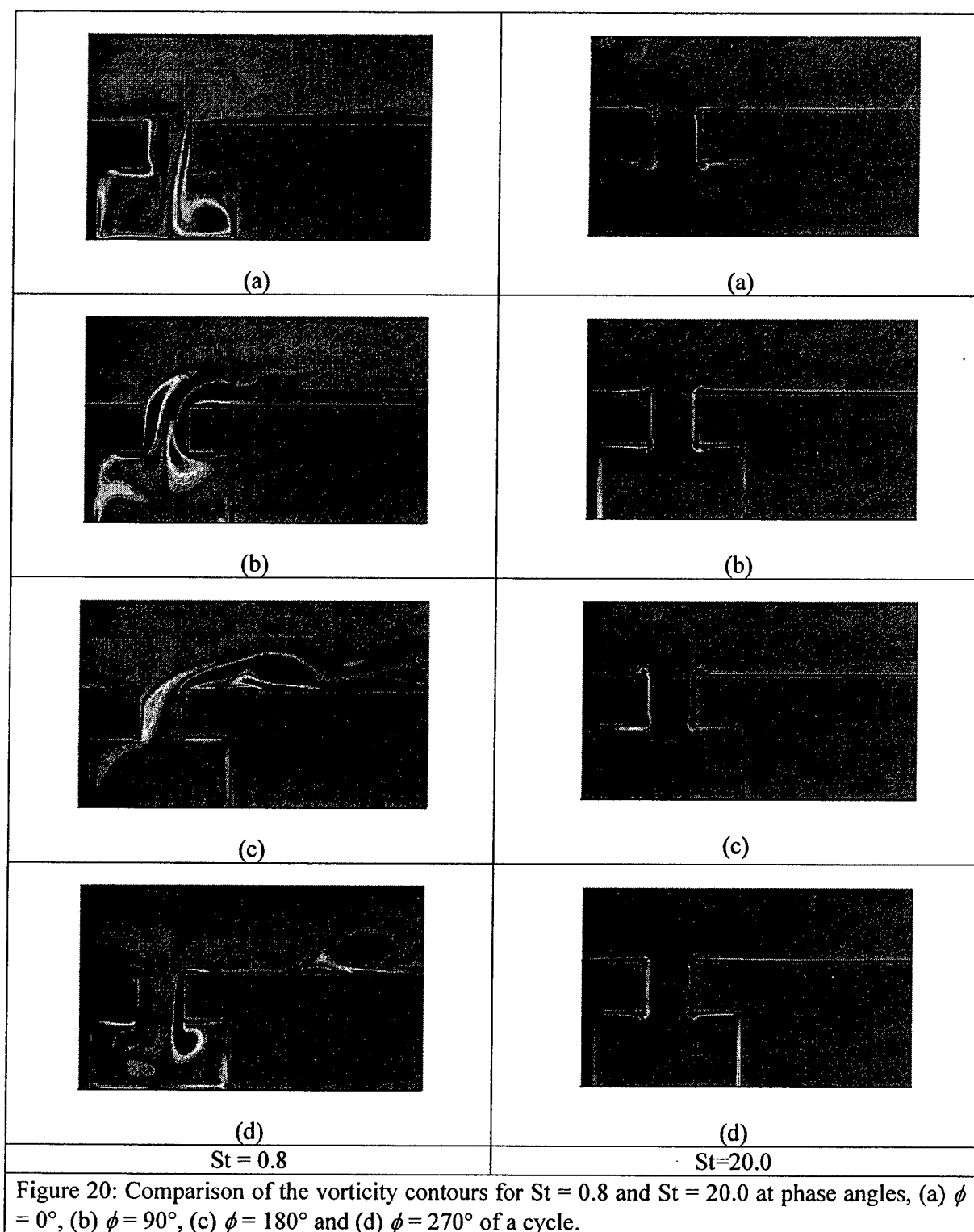
where, δ/d and $U_\infty/\overline{V}_J$ are dependent on the incoming boundary layer.

Here we report some of the preliminary findings for developing this scaling law. 2-D computations have been performed for simplified geometry for ZNMF actuator for fixed cavity width ($W/D = 3$) and slot height ($h/d = 1$). Functional dependencies are studied by varying one of the parameters with the others held fixed. Due to the extensive range of the probabilities, we have chosen relatively low Reynolds number cases for preliminary studies. The range of the same has been in listed in Table 3.

Table 3. Range of parameters varied

Parameters	Range
δ/d	$0.5 - 3.0$
$U_\infty/\overline{V}_J$	$0.5 - 4.0$
Re_j	$93.75 - 500$

This set of calculations yield a range of Reynolds number based on the boundary layer thickness ($Re_\delta = U_\infty \delta/\upsilon$) of 125 - 4000 while for that of Strouhal number, St is found to be $0.1 - 26.7$. It is found that during the expulsion phase the actuator expels vortices which essentially trip the boundary layer in the proximity of the jet. In the process vortices formed are carried further downstream by the interacting boundary layer. Figure 20 shows the vorticity contours of a synthetic jet interacting with the laminar boundary at $Re_\delta=1000$ for St = 0.8 and 20.0. For St = 0.80 ($Re_j = 125$, S = 10) the expelled vortices are swept away by the laminar boundary layer. For the same $Re_j = 125$, at significantly high Stokes number (S=20) the vortices formed are not completely expelled, and are ingested back as seen in Figure 20. This indicates that for sufficiently high St the vorticity flux might not be having a significant affect on the boundary layer.

23

(a)	(a)
(b)	(b)
(c)	(c)
(d)	(d)
St = 0.8	St=20.0

Figure 20: Comparison of the vorticity contours for St = 0.8 and St = 20.0 at phase angles, (a) ϕ = 0°, (b) ϕ = 90°, (c) ϕ = 180° and (d) ϕ = 270° of a cycle.

The normalized instantaneous vorticity flux, $\Omega(t) = \int_0^{d/2} \xi_z u \, dy$ based on the magnitude of vorticity across the slot exit, has been shown in Figure 21(a) as function of phase for St = 3.2 and $U_\infty / \overline{V}_J = 4$. For fixed $Re_j = 125$ and $S = 10$ (St = 3.2), the time averaged vorticity flux is plotted as a function of δ/d in Figure 21(b). For very low values of δ/d as expected there is a high magnitude of vorticity which decreases towards to an asymptotic with an increase in the boundary layer thickness. For $\delta/d > 2$ this variation is marginal indicating that the vortices are not able to penetrate boundary layer at these values.
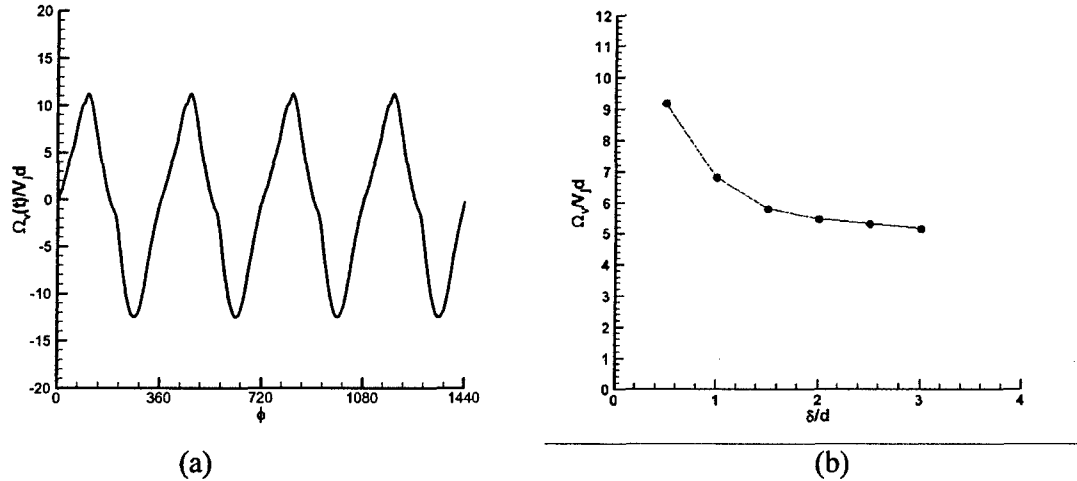

(a)   (b)

Figure 21: (a) Normalized $\Omega_v(t)$ across the slot exit as a function of the phase for four cycles, (b) normalized Ω_v across the slot exit as a function of the varying δ/d.

Figure 22(a) shows the variation of the vorticity flux Ω_v with increasing St. Here St has been varied from 0.10 to 26.67 for four different Re_j's while fixing $U_\infty / \overline{V}_J = 4$. The plot shows an almost a linear behavior of Ω_v with respect to St for all the Reynolds numbers. This is similar to the experimental findings for quiescent flows. On the other hand the vorticity flux shows a weak dependence on $U_\infty / \overline{V}_J$ over a range of 0.5 to 4 with the other parameters fixed, seen in Figure 22(b). We are currently analyzing the data for a power law type scaling, $\dfrac{\Omega_v}{\overline{V}_J d} = \beta . St^\lambda \left(\dfrac{U_\infty}{\overline{V}_J}\right)^\sigma$,

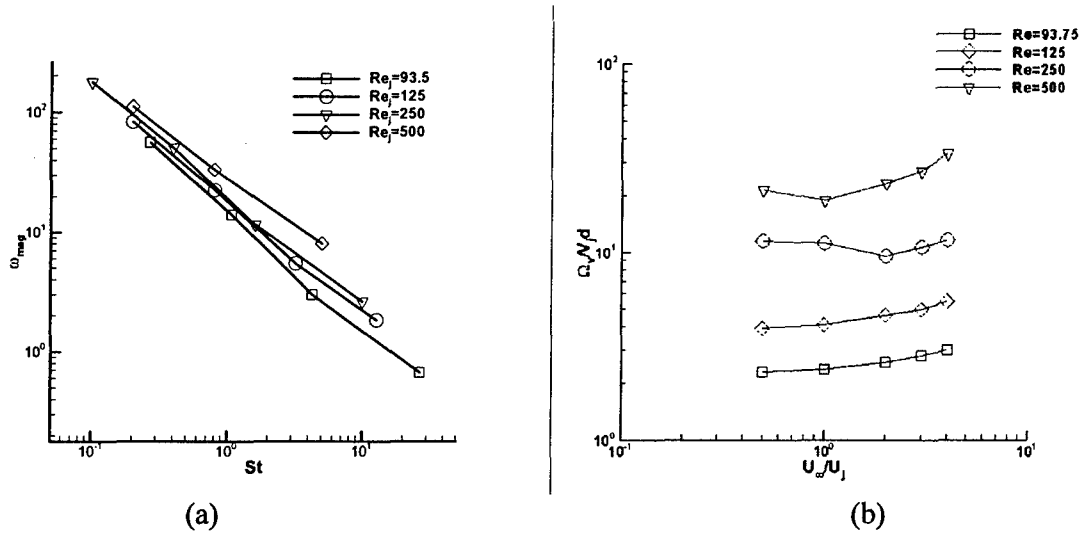where β, λ and σ are to be determined.

25

Figure 22: Vorticity flux as a function of (a) Strouhal number and (b) $U_\infty / \overline{V}_J$ at different Re_j's.

d. Entrance Length in Oscillatory Slot Flows

The ratio of pressure drop to volume flow rate, $\Delta p / Q$, called impedance, is an important factor in low-order models of synthetic jets. The entrance/inlet length of a flow is defined as the distance from the inlet section of a channel to the point where the velocity becomes independent of entrance effects. The flow in the slot of a synthetic jet is analogous to the entrance length of a channel in oscillatory flow. Since the slot height to width ratio in ZNMF actuators is comparable, the flow is generally not fully developed in the slot region. Development length would thus significantly affect the loss coefficients in the slot. Obtaining an analytical expression for the same would directly impact the ongoing work of low-dimensional modeling for ZNMF devices.

Unsteady pipe and channel flows, both oscillatory and pulsatile, have been under investigation for a long period of time due to its applications in mostly biological systems. The oscillatory flows have a zero mean velocity where the velocity is generally given as $u = u_o\sin\omega t$; whereas pulsatile flows with $u = u_o + \sin\omega t$ have a non-zero mean velocity. Although several researchers have extensively investigated entrance effects in steady flows (Sparrow et al., 1964; Van Dyke, 1970; Fargie & Martin, 1971; Chen, 1973 and Narang & Krishnamoorthy, 1976) and pulsatile flows (Atabek & Chang, 1961 and He & Ku, 1994) only a few have documented these effects for purely oscillatory flows (Kassianides & Gerrad, 1975 and Goldberg & Folk, 1988). In the current study we develop a semi-analytical model for predicting the entrance losses and use numerical simulations to provide empirical data for the closure of the semi-analytic model. For this purpose two types of channel configurations were chose. Figure 23(a) shows a straight channel with an oscillatory velocity profile prescribed at the inlet while in order to extend the application of the model to synthetic jets a channel with sharp-corners at the entrance was chosen, Figure 23(b). Similar configuration has been used earlier entrance losses for steady flow calculations (Sadri & Floryan, 2002), to our knowledge, not for oscillatory flows.
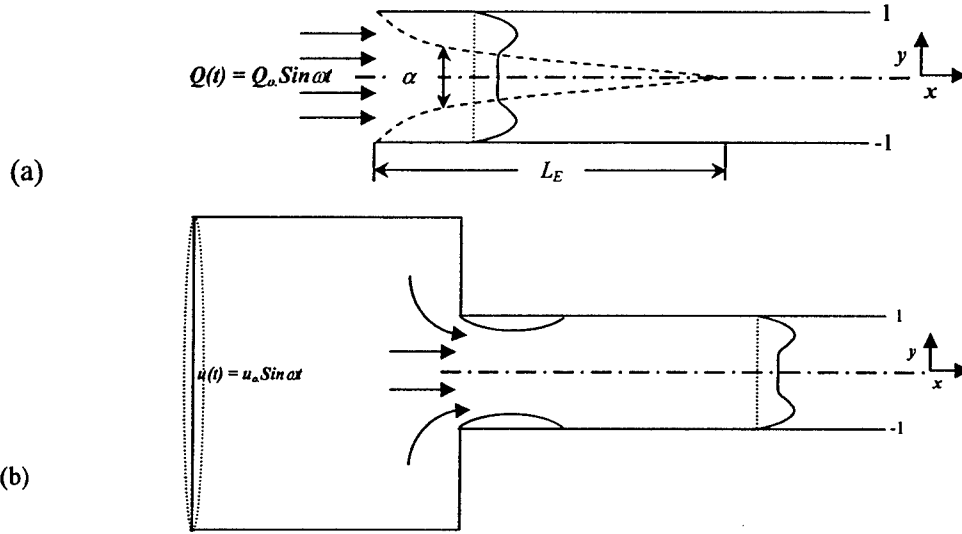
26

Figure 23: Schematic of entrance flow in a (a) straight channel and (b) channel with a sharp-corners.

The governing equations for flow through 2-D channel of height, h with rigid walls as seen in Figure 23(a), can be non-dimensionalized based on the Stokes number, S. Assuming there is no cross-component of the velocity and integrating across a section of the channel the N-S equations can be simplified in terms of the axial velocity, u as,

$$S^2 \frac{\partial Q}{\partial t} + \frac{\partial}{\partial x} \int_{-1}^{1} u^2 dy = -\frac{\partial \overline{P}}{\partial x} + \frac{\partial u}{\partial y}\bigg|_1$$

where $Q(t)$ and $\overline{P}$ are the volumetric flow rate and average pressure across the channel height respectively.

We assume a profile of the axial velocity of the following form based on the analytical solution for developing laminar steady flow in a channel given by Fargie and Martin (1971),

$$u = \begin{cases} u_o(t) & \text{for } 0 \le y \le \alpha(x) \\ u_o(t)f(\alpha,y,S) & \text{for } \alpha(x) \le y \le 1 \end{cases}$$

where, $f(\alpha,y,S) = \text{Real}\left[\dfrac{\cosh(S') - \cosh(S'z)}{\cosh(S') - 1}\right]$ based on the theoretical model given for unsteady fully-developed flows by Loundon and Tordesillas (1998), $u_o(t)$ is the oscillatory velocity, $\alpha(x)$ is the core length $((1-\alpha)$ is the boundary layer thickness) , $S' = S\sqrt{i}$ and $z = y - \alpha/1 - \alpha$.

The continuity equation yields the form of $u_o(t)$ based on $K_l(S)$,a known integral function of S as,

$$u_o(t) = \frac{Q(t)}{2(\alpha + (1 - \alpha)K_1(s))}$$

27

This yields a final form of the solution for the pressure loss by integration over the entrance length L_E as,

$$\overline{P}_{L_E} - \overline{P}_0 = -\frac{S^2}{2}\frac{\partial Q}{\partial t}L_E - \frac{Q^2}{4}\left[\frac{K_2(S)}{(K_1(S))^2}-1\right]-\frac{QK_3(S')}{2}\int_0^{L_E}\frac{dx}{(1-\alpha)(\alpha+(1-\alpha)K_1(S))}$$

where K_2 and K_3 are again known integral functions of S. The first term on the RHS represents the loss coefficient due to the inviscid acceleration, the second due to *entrance loss* from the convective term and the third are due to the viscous effects. Hence we can obtain a closed form expression for determining the loss coefficients in the entrance length of a channel.

The key unknown for the closed form expression is the core length $\alpha(x)$ which essentially is a function of the entrance length L_E. The entrance length for pulsatile flows is given as $L_E/h = 2.64/St$ when an oscillation is superimposed on a steady flow (Fung, 1997). This shows that the entrance length for these flows is inversely proportional to the Strouhal number. The objective here is to develop similar scaling law for a purely oscillatory flow using numerical simulations, which then would be used to obtain an expression for $\alpha(x)$.

Presently we are examining entrance lengths in 2-D channel flows with low Reynolds number ranging from 50 to 1000 and Stokes number from 5 to 50, since the synthetic jets operate in this range. These studies are being carried out on grids ranging from 54-107 and 251-1001 grid points in spanwise and streamwise directions respectively. Grid dependence studies showed the results match within 0.4 %. Oscillatory boundary condition was prescribed at the inlet with no-slip boundary conditions on the walls. Data over the first half of the cycle was evaluated and entrance length was calculated based on the length in the streamwise direction where the velocity reaches 99% of its peak value. Figure 24(a-b) show the entrance length as a function of phase for Re = 50 and Re = 250 respectively for five different Stokes number. Comparison shows that L_E is a dependent on both Re and S; higher values lead to longer entrance lengths. Figure 25(a) plots the normalized average entrance length as a function of S for three different Re ranging from 50 to 250. It shows a rapid decay for higher S converging to an asymptotic value of L_E. Comparison of the average entrance length with St for the same range of Re shows a collapse suggesting the flow might become Re independent at higher values of St, as seen in Figure 25(b).
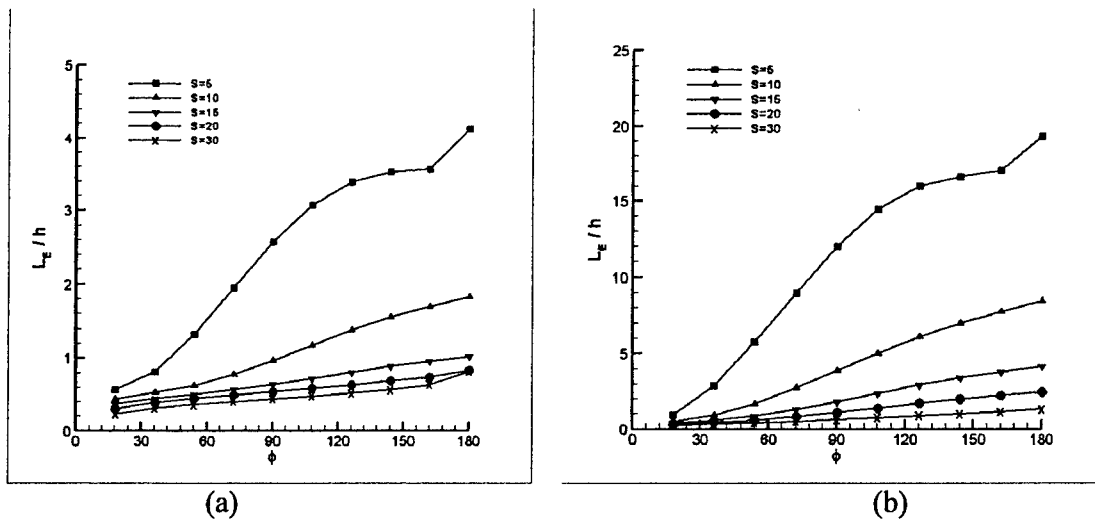
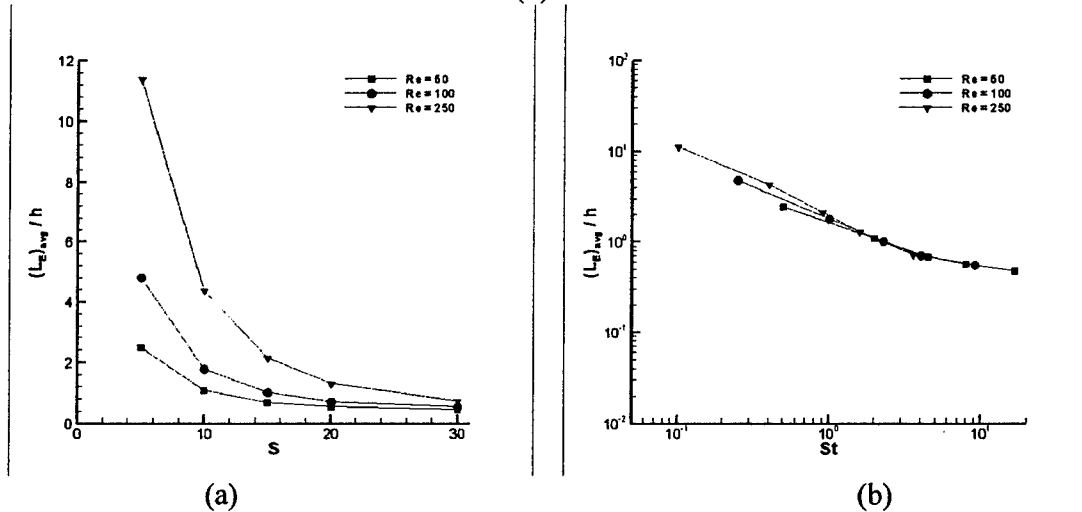Figure 24: Entrance length variation as a function of phase for varying Stokes number at (a) Re = 50 and (b) Re = 250.

Figure 25: Average entrance length as a function of (a) Stokes number, and (b) Strouhal number.

Bibliography

1.   Amitay, M., Honohan, A., Trautman, M., and Glezer, A., "Modification of the Aerodynamic Characteristics of Bluff Bodies Using Fluidic Actuators," *AIAA* 97-2004, 1997.

2.   Amitay, M., Kibens, V., Parekh, D., and Glezer, A., "The Dynamics of Flow Reattcahment Over a Thick Airfoil Controlled by Synthetic Jet Actuators," *AIAA* 99-1001, 1999.

3.   Atabek, B.H and Chang, C.C., "Oscillatory flow near the entry of a circular tube," *Z.f.angew.Math & Phys.*, Vol. 12, pp.185, 1961.

4.   Bozkurttas, M., Dong, H., Seshadri, V., Mittal, R., Najjar,F. "Towards Numerical Simulation of Flapping Foils on Fixed Cartesian Grids, " AIAA 43rd Aerospace Sciences Meeting and Exhibit, Jan 10-13, Reno, Nevada, AIAA 2005-0079

5.   Chen, R.Y., "Flow in the Entrance Region at Low Reynolds Numbers," *ASME J. Fluids Eng.*, Vol. 95, pp. 153-158, 1973.

6.   Chen, Y., Liang, S., Anug, K., Glezer, A. and Jagoda, J., "Enhanced mixing in a Simulated Combustor Using Synthetic Jet Actuators," *AIAA* 99-0449, 1999.

7.   Crook, A., Sadri, A. M., and Wood, N. J., "The Development and Implementation of Synthetic Jets for the Control of Separated Flow," *AIAA* 99-3176, 1999.

8.   Crook, A. and Wood, N.J., "Measurements and Visualizations of the Synthetic jets," *AIAA* 01-0145, 2001.

9.   Davis, S.A. and Glezer, A., "Mixing Control of Fuel jets using Synthetic jets Technology: Velocity Field measurement," *AIAA* 99-0447, 1999.

10. Fargie, D. and Martin, B.W., "Developing laminar flow in a pipe of circular cross-section," *Proceedings of the Royal Society of London, Series A, Mathematical and Physical Sciences*, Vol. 321 (1546) ,pp. 461-476, 1971.

11. Fung, Y. C. "Biomechanics circulation," 2nd edition, *Springer-Velag*, pp. 188-189, 1997.

12. Gallas, Q., Holman, R., Nishida, T., Caroll, B., Sheplak, M. and Cattafesta, L., "Lumped Element modeling of Piezoelectric-Driven Synthetic Jet Actuators," *AIAA Journal*, Vol. 41, No. 2, pp. 240-247, 2003.

13. Gallas, Q., Holman, R., Raju, R., Mittal, R, Sheplak, M., and Cattafesta, L., "Low Dimensional Modeling of Zero-Net Mass-Flux Actuators," *AIAA* 2004-2413, 2004.

14. Goldberg, I.S. and Folk, R.T., , "Solutions for Steady and Nonsteady Entrance Flow in a semi-infinite circular tube at very Low Reynolds number," *ASME Journal of Applied Mathematics*, Vol. 48, pp. 770, 1988.

15. He, Y.Y., Cary, A.W. and Peters, D.A., " Parametric and Dynamic modeling for Synthetic Jet Control of a Post-Stall Airfoil," *AIAA* 01-0733, 2001.

16. He,X. and Ku, D.N., "Unsteady entrance flow development in a straight tube," *Journal of Biomechanical Eng.*, Vol. 116(3),pp. 355-60, 1994.

17. Hinze, J. O., *Turbulence*, McGraw-Hill, 1975.

18. Kassianides, E. and Gerrad, J.H., "Calculation of Entrance length in Physiological flow," *Medical and Biological Engineering*, pp. 558, 1975.

19. Lee, C. Y. and Goldstein, D. B., "DNS of Microjets for Turbulent Boundary Layer Control," *AIAA* 01--1013, 2001.

20. Leonard, B. P., "A Stable and Accurate Convection Modeling Procedure Based on Quadratic Upstream Interpolation," *Comput. Methods Appl. Mech. Engrg.*, Vol. 19, 1979, pp. 59--98.

21. Loudon, C. and Tordesillas, A. "The use of the dimensionless Womersley number to characterize the unsteady nature of internal flow," *Journal of Theoretical Biology*, Vol.191, pp. 63-78, 1998.

22. Najjar, F. M. and Mittal, R., "Simulations of Complex Flows and Fluid-Structure Interaction Problems on Fixed Cartesian Grids," FEDSM2003--45577, *Proc. FEDSM'03, 4th ASME-JSME Joint Fluids Engineering Conference*, Honolulu, Hawaii, 2003, pp.184-196.

23. Narang, B.S., and Krishnamoorthy, G., "Laminar Flow in the Entrance Region of Parallel Plates," *ASME J. Appl. Mech.*, Vol. 43, pp. 186-188, 1976.

24. Rathnasingham, R. and Breuer, K. S., "System Identification and Control of a Turbulent Boundary Layer," *Phys. Fluids A*, Vol. 9, No. 7, 1997, pp. 1867--1869.

25. Rathnasingham, R. and Breuer, K. S., "Active Control of Turbulent Boundary Layers," *J. Fluid Mech.*, Vol. 495, 2003,

26. Sadri, R.M. and Floryan, J.M., " Accurate evaluation of the Loss coefficient and the Entrance length of the inlet region of a channel," *Journal of Fluids Engineering*, Vol. 124, pp. 685-693.

27. Smith, D., Amitay, M., Kibens, V., Parekh, D., and Glezer, A., "Modification of Lifting Body Aerodynamics Using Synthetic Jet Actuators," *AIAA* 98-0209, 1998.

28. Smith, B. L. and Glezer, A., "Vectoring and Small-Scale Motions Effected in Free Shear Flows Using Synthetic Jet Actuators," *AIAA* 97-0213, 1997.

29. Smith, B. L. and Glezer, A., "The Formation and Evolution of Synthetic Jets, *Phys. Fluids*, Vol. 10, No. 9, 1998, pp. 2281--2297.

30. Smith, B. L., and Swift, G. W., "Power Dissipation and Time-Averaged Pressure in Oscillating Flow Through a Sudden Area Change," *J. Acoust. Soc. Am.*, Vol. 113, No. 5, May 2003.

31. Sparrow, E.M. and Lin, S.H., "Flow Development in the Hydrodynamics Entrance Region of Tubes and Ducts," *Physics of Fluids*, Vol. 7, pp.338-347, 1964.

32. Tennekes, H. and Lumley, J. L., *A First Course in Turbulence,* The MIT Press, 1972.

33. Utturkar, Y., "Numerical Investigation of Synthetic Jet Flow Fields," *MS Thesis, Department of Mechanical Engineering, University of Florida*, 2002.

34. Utturkar, Y., Holman, R., Mittal, R., Carroll, B., Sheplak, M., and Cattafesta,L., "A Jet Formation Criterion for Synthetic Jet Actuators," *AIAA* 03-0636, 2003.

35. Van Dyke, M., "Entry flow in a Channel," *J. Fluid Mechanics*, Vol. 44, pp. 813-823, 1970.

36. Wygnanski, I., "Boundary Layer and Flow Control by Periodic Addition of Momentum," *AIAA* 97-2117, 1997.

37. Yao, C. S., Chen, F. J., Neuhart, D., and Harris, J., "Synthetic Jets in Quiescent Air," *Proc. NASA LaRC Workshop on CFD Validation of Synthetic Jets and Turbulent Separation Control*, Williamsburg, Virginia, March 29-31, 2004.

38. Ye, T., Mittal, R., Udaykumar, H. S., and Shyy, W., "An Accurate Cartesian Grid Method for Viscous Incompressible Flows with Complex Immersed   Boundaries, *J. Comp. Phys.*, Vol. 156, 1999, pp. 209-240.

39. Yehoshua, T. and Seifert, A. "Boundary Condition Effects on Oscillatory Momentum Generator," *AIAA* 03-3710, 2003.

40. Zang, Y., Street, R. L., and Kossef, J. R., "A non-staggered Grid, Fractional Step Method for Time-Dependent Incompressible Navier-Stokes Equations in Curvilinear Coordinates," *J. Comp. Phys.*, Vol. 114, 1994, pp. 18--33.

IV. Personnel Supported

Dr. Rajat Mittal (Professor)
Dr. Haibo Dong (Research Scientist)
Reni Raju (Graduate Student)
Rupesh B. Kotapati (Graduate Student)

V. Publications Resulting from the Grant

1. Raju, R., Mittal, R., Gallas, Q. and Cattafesta III, L.N., "Scaling of Vorticity Flux and Entrance Length Effects in Zero-Net Mass-Flux devices," AIAA 2005-4751, June 2005.

2. Mittal, R., Iaccarino, G., "Immersed Boundary Methods," Annual Review of Fluid Mechanics, Vol. 37, pp.239-261, 2005.

3. Mittal, R., Kotapati, R.B., Cattafesta III, L.N., "Numerical Study of Resonant Interactions and Flow Control in a Canonical Separated Flow," AIAA 2005-1261, 2005.

4. Kotapati, R.B., Mittal, R., "Time-Accurate Three-Dimensional Simulations of Synthetic Jets in Quiescent Air," AIAA 2005- 0103, 2005.

5. Mittal, R., Kotapati, R.B., "Resonant Mode Interaction in a Canonical Separated Flow, " IUTAM Symposium on Laminar-Turbulent Transition, 13-17 December 2004, Bangalore, India.

6. Gallas, Q., Holman, R., Raju, R., Mittal, R, Sheplak, M., and Cattafesta, L., "Low Dimensional Modeling of Zero-Net Mass-Flux Actuators," AIAA 2004-2413, 2004.

7. Ravi, B., R. Mittal, R., and Najjar, F., M. "Study of Three-Dimensional Synthetic Jet Flowfields using Direct Numerical Simulation," AIAA 2004-0091, 2004.

VI. Interactions

1. Mittal, R., Kotapati, R.B., Cattafesta III, L.N., "Numerical Study of Resonant Interactions and Flow Control in a Canonical Separated Flow," AIAA 43rd Aerospace Sciences Meeting and Exhibit, Reno, Nevada, Jan 10-13, 2005.

2. Kotapati, R.B., Mittal, R., "Time-Accurate Three-Dimensional Simulations of Synthetic Jets in Quiescent Air," AIAA 43rd Aerospace Sciences Meeting and Exhibit, Reno, Nevada, Jan 10-13, 2005.

3. Mittal, R., Kotapati, R.B., "Resonant Mode Interaction in a Canonical Separated Flow, " IUTAM Symposium on Laminar-Turbulent Transition, Bangalore, India,13-17 December 2004.

4. Rupesh, R.B., Ravi, B. R., Raju, R. , Mittal, R., , Gallas, Q. and Cattafesta, L., "Case 1: Time-Accurate Numerical Simulations of Synthetic Jets in Quiescent Air," NASA LaRC Workshop on CFD Validation of Synthetic Jets and Turbulent Separation Control, 29-31 March, 2004, Williamsburg, Virginia.

5. Ravi, B., R. Mittal, R., and Najjar, F., M. "Study of Three-Dimensional Synthetic Jet Flowfields using Direct Numerical Simulation," 42nd AIAA Aerospace Sciences Meeting and Exhibit, Reno, Nevada, 5-8 January 2004.